Pharmaceutical Research, Vol. 22, No. 2, February 2005 (© 2005)
DOI: 10.1007/s01869-005-1869-8

Research Paper

Estimation of the Three-Dimensional Pharmacophore of Ligands for Rat Multidrug-Resistance–Associated Protein 2 Using Ligand-Based Drug Design Techniques

Shuichi Hirono,[1,3] Izumi Nakagome,[1] Rie Imai,[1] Kazuya Maeda,[2] Hiroyuki Kusuhara,[2] and Yuichi Sugiyama[2]

Received March 22, 2004; accepted July 19, 2004

Purpose. Multidrug-resistance–associated protein 2 (Mrp2) shows a broad substrate specificity toward amphiphilic organic anions. This study identified key functional groups of ligand molecules for binding to rat Mrp2, determined their relative locations, and examined substrate specificity through receptor mapping using three-dimensional (3D) quantitative structure-activity relationship (3D-QSAR) analysis.
Methods. Ligand-binding conformations were estimated using conformational analysis (CAMDAS) and molecular superposition (SUPERPOSE) methods to clarify the substrate specificity of rat Mrp2 in relation to 3D ligand structures.
Results. Two types of binding conformations of ligands for rat Mrp2 were identified. 3D-QSAR comparative molecular-field analysis (CoMFA) revealed a statistically significant model for one type, in which the steric, electrostatic, and log P contributions to the binding affinity for rat Mrp2 were 63.0%, 33.4%, and 3.6%, respectively ($n = 16$, $q^2 = 0.59$, $n = 3$, $r^2 = 0.99$, and $s = 0.08$).
Conclusions. The 3D pharmacophore of ligands for rat Mrp2, and the ligand-binding region of rat Mrp2, were estimated. Ligand recognition of rat Mrp2 is achieved through interactions in two hydrophobic and two electrostatically positive sites (primary binding sites). The broad substrate specificity of rat Mrp2 might result from the combination of secondary (two electrostatically positive and two electrostatically negative sites) and primary binding sites.

KEY WORDS: binding conformation; 3D pharmacophore; 3D-QSAR; rat Mrp2; substrate specificity.

INTRODUCTION

The liver is one of the most important organs in the detoxification of xenobiotics, and biliary excretion is a major pathway for their elimination. Compounds in the circulating blood are taken up by hepatocytes and are then metabolized and/or excreted into the bile. Many kinds of drugs and their metabolites are transported across the sinusoidal and bile canalicular membranes via carriers. The mechanism of transport across the bile canalicular membrane has been characterized using isolated canalicular membrane vesicles (CMVs), which revealed that several types of primary active transporters are responsible for ligand efflux from the hepatocytes into the bile. Among them, multidrug-resistance–associated protein-2 (Mrp2; gene symbol ABCC2) has an important role in the biliary excretion of many organic anions and glutathione or glucuronide conjugates (1–3).

Mrp2 is an ATP-binding cassette (ABC) transporter, which possesses two highly conserved ABC regions. The Eisai hyperbilirubinemic rat (EHBR), which has a hereditary Mrp2 deficiency owing to the insertion of a nonsense mutation (4), and the GY/TR$^-$ rat (5) have both helped to reveal the importance of Mrp2 in the biliary excretion of various types of organic anions. In the EHBR, the biliary excretion of Mrp2 substrates is drastically decreased, and the ATP-dependent uptake of Mrp2 substrates into CMVs prepared from EHBRs is greatly reduced compared with those prepared from normal rats.

These findings demonstrate that a wide range of organic anions can be substrates for Mrp2, which include: nonconjugated organic anions such as dibromosulfophthalein (6,7), cefodizime (β-lactam antibiotic) (7), pravastatin (a 3-hydroxy-3-methyl-glutaryl-coenzyme A reductase inhibitor) (8), temocaprilat (an angiotensin-converting enzyme inhibitor) (9), the carboxylate forms of CPT-11 and its active metabolite (SN-38, which is a topoisomerase inhibitor) (8), and a cyclic anionic peptide (BQ-123, which is an endothelin antagonist) (10); glutathione conjugates such as leukotriene C_4 (11) and DNP-SG (12); and glucuronide conjugates such as bilirubin glucuronide (13), E3040 glucuronide (14,15), and SN-38 glucuronide (16).

[1] School of Pharmaceutical Sciences, Kitasato University, Tokyo 108-8641, Japan.
[2] Graduate School of Pharmaceutical Sciences, University of Tokyo, Tokyo 113-0033, Japan.
[3] To whom correspondence should be addressed. (e-mail: hironos@pharm.kitasato-u.ac.jp)

ABBREVIATIONS: ABC, ATP-binding cassette; CAMDAS, Conformational Analyzer with Molecular Dynamics and Sampling; C log P, calculated log P; CMVs, canalicular membrane vesicles; CoMFA, comparative molecular-field analysis; EHBR, Eisai hyperbilirubinemic rat; MD, molecular dynamics; Mrp2, multidrug-resistance-associated protein 2; PLS, partial least squares; QSAR, quantitative structure-activity relationship; rmsd, root-mean-square deviation; SD, Sprague-Dawley.

Clearly, rat Mrp2 accepts many organic anions as substrates. However, its broad substrate specificity has not been investigated in terms of the three-dimensional (3D) structures of ligands (17), and the complete 3D structure has not been determined for any mammalian transporter. Elucidating the structural characteristics of the ligand-binding region of rat Mrp2 would be useful for understanding its broad substrate specificity. Therefore, in the current study, we investigated the binding conformation of ligands to rat Mrp2, the key functional groups for binding to Mrp2 (3D pharmacophore), and the 3D quantitative structure-activity relationships (3D-QSAR) between ligands and rat Mrp2. Our combined method comprised the following three procedures: first, conformational analysis (CAMDAS) (18); second, a molecular superposition procedure (SUPERPOSE) (19); and third, 3D-QSAR analysis by comparative molecular-field analysis (CoMFA) (20). These techniques are described in more detail in the following section.

MATERIALS AND METHODS

Conformational Analysis: Sampling of a Set of Conformers of a Molecule

X-ray structural analysis of protein-ligand complexes has revealed that the binding conformation is one of the stable conformations of a ligand molecule. To generate a set of conformers of ligands, we used the automated program Conformational Analyzer with Molecular Dynamics and Sampling (CAMDAS), which was developed by Tsujishita and Hirono (18). CAMDAS performs high-temperature molecular dynamics (MD) calculations for a target molecule and for sampled conformers that appear during the MD. It then evaluates the similarities between each of the sampled conformers in terms of dihedral angle values, clusters similar conformers together, and, finally, prints out the clustered conformers. In this way, CAMDAS can find the representative conformers from an arbitrarily given structure of the molecule.

To estimate the binding conformation of ligands to rat Mrp2, MD dynamics calculations were executed for 18 ligands (a training set for constructing QSAR models comprising compounds **1–16** and a test set for verifying the QSAR models comprising compounds **A** and **B**), and many conformers were sampled; their chemical structures are shown in Figs. 1 and 2. An MD calculation for sampling was performed for 800 ps with an integral time step of 0.001 ps using an MM2 force field (21) without electrostatic and hydrogen-bonding interactions. The temperature of the system was maintained at 1200 K, and the length of the covalent bonds was fixed using the SHAKE algorithm throughout the MD simulations. Conformers were sampled at every 100 steps and preclustered with dihedral angles during the MD simulations. If the difference between conformers was within ±30°, they were grouped together. Subsequently, reclustering of the sampled conform-

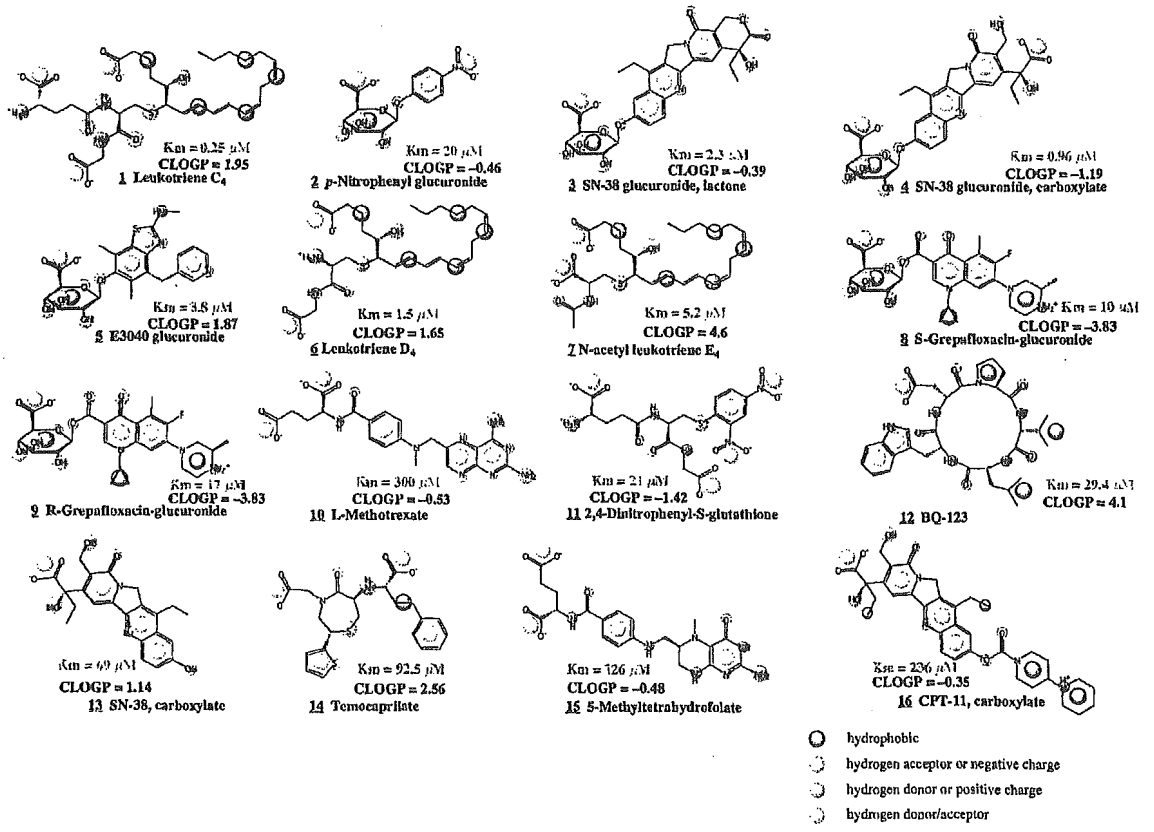

Fig. 1. Chemical structures of the compounds in the training set, with property spheres, K_m, and C log P values.

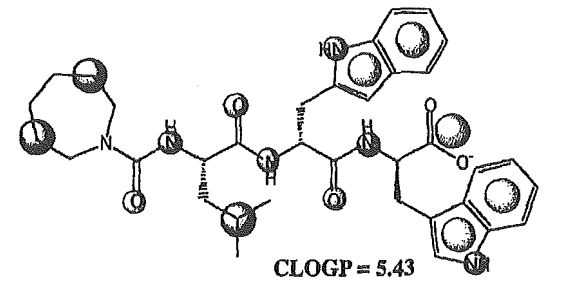

CLOGP = 5.43
A BQ-485 Km = 6.46 μM

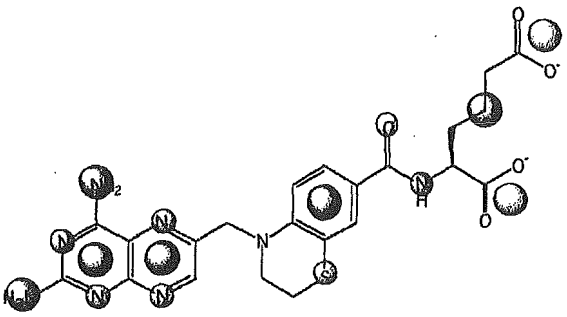

CLOGP = 0.61
B MX-68 Km = 207 μM

hydrophobic
hydrogen acceptor or negative charge
hydrogen donor or positive charge
hydrogen donor/acceptor

Fig. 2. Chemical structures of the compounds in the test set, with property spheres, K_m, and C log P values.

ers was performed with dihedral angles within ±30°. Before the clustering, each conformer was minimized until the root-mean-square (rms) of the gradients of the potential energy was below 0.004 kcal mol^{-1} $Å^{-1}$.

Molecular Superposition: Selection of the Candidate Binding Conformations

X-ray crystallographic studies of protein-ligand complexes have demonstrated that when ligands bind to a given protein, such as a receptor or a transporter, the atomic groups in the ligands that interact with amino-acid residues of the protein occupy the same 3D space. Based on this information, we carried out molecular superposition for ligand molecules using the SUPERPOSE program developed by Iwase and Hirono (19). The program superposes two molecules based on the physicochemical properties of the atomic groups, which is useful for elucidating a pharmacophore and estimating a binding conformation by distinguishing it from among the many conformations that are generated by high-temperature MD calculations.

Five types of physicochemical properties are considered in the program, including hydrophobic (aromatic), hydrogen-bond donors, hydrogen-bond acceptors, and hydrogen-bond donors/acceptor. Each type is represented as a sphere with a predefined radius and is assigned to a functional group in a molecule. After molecular superposition, the overlaps of the spheres are scored.

The program works as follows. First, a large molecule with its physicochemical properties represented by spheres is fixed at the center of a large box, and another smaller molecule, also with spheres representing its physicochemical properties, is translated and rotated in the box. The translational increment is 1 Å, and the center of mass is translated onto the body-centered-cubic lattice-points made in the circumscribed large-volume rectangular box. The rotation is performed on each of the lattice points. The ranges of the three Eulerian angles are $0° \leq \phi, \varphi < 360°$, and $0° \leq \theta \leq 180°$. The rotational increment is 4°. Second, at every translation or rotation, the property spheres that overlap are determined by calculating the distances between the spheres of the molecules. Third, overlaps of the spheres are scored so that points are added when atomic groups with the same physicochemical properties overlap, and points are subtracted when atomic groups with different physicochemical properties overlap, according to the scoring table (19). Atomic groups without overlaps are not scored.

These three operations are repeated to determine the orientation with the highest score and the smallest rms deviation (rmsd) of the distances of the overlapped atomic groups between the two molecules.

3D-QSAR Analyses: Determination of the Binding Conformation Using CoMFA

The SUPERPOSE program identified several plausible binding conformations. We therefore carried out comparative molecular field analysis (CoMFA) to determine the binding conformation of ligands to rat Mrp2 and to obtain 3D structure-activity relationships.

Table I. Results of Conformational Analysis by CAMDAS

	Number of conformers	ΔE (kcal/mol)	Number of conformers within 12 kcal/mol
Training set			
1	7777	15.570	3846
2	16	14.406	15
3	262	18.565	234
4	876	18.877	798
5	251	16.972	240
6	7777	13.951	5723
7	3121	1112.579	1576
8	479	54.432	316
9	264	32.593	180
10	2547	1013.488	2387
11	3957	978.039	3530
12	5937	53.872	1533
13	177	13.669	176
14	3078	52.334	2832
15	3069	1028.764	2915
16	5135	32.084	3856
Test set			
A	36	480.492	20
B	7777	86.823	4966

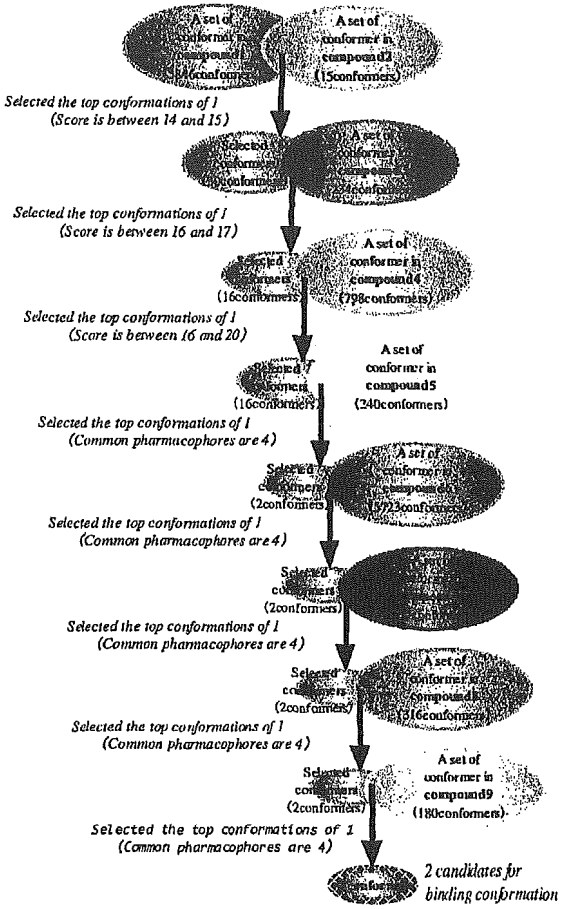

Fig. 3. Flowchart of SUPERPOSE.

The atomic charges of each conformer were calculated using the semiempirical molecular orbital program package MOPAC93 MNDO/ESP, in order to evaluate the electrostatic field in CoMFA. Conventional CoMFA was performed using the QSAR option of SYBYL (Tripos, Inc., St. Louis, MO, USA), with the Michaelis constant (K_m) (22) of each ligand included as bioactive data, as shown in Figs. 1 (training set) and 2 (test set). For the K_m-determination experiments, CMVs were prepared from male Sprague-Dawley (SD) rats, and the transport study was performed using the rapid-filtration technique, as described previously (11,12). All of the compounds were mainly excreted into the bile via rat Mrp2, as biliary excretion in EHBRs and/or the ATP-dependent uptake of each compound into CMVs prepared from EHBRs was disrupted. Therefore, the K_m values for the uptake into CMVs prepared from SD rats corresponded to those for rat Mrp2.

Two calculations were carried out, using an sp^3 carbon probe atom with a charge of +1 and either the steric and electrostatic components or the steric, electrostatic, and calculated log P (C log P) components. The calculated values of log P were estimated using the CLOGP program (Daylight, C.I.S. Inc., Rochester, NY, USA). The CoMFA QSAR equations were calculated with the partial least squares (PLS) algorithm. The optimal number of components in the final CoMFA PLS model was determined using the cross-validated R^2 (q^2) values obtained from the leave-one-out cross-validation technique. The CoMFA PLS model with the highest q^2 values was selected to estimate the binding conformation of ligands for rat Mrp2.

RESULTS

Sampling of a Set of Conformers of Each Ligand

Using the CAMDAS program, we carried out conformational analyses of ligand molecules bound to rat Mrp2. The high-temperature MD calculation was used with a potential function without an electrostatic interaction term and a hydrogen-bonding term to avoid undesirable intramolecular interactions (Figs. 1 and 2). The CAMDAS calculations gave many conformers of the 18 compounds, as shown in Table I. The sets of conformers of compounds **1–9**, the structures of which were significantly different from one another and showed relatively low K_m values, were used by the SUPERPOSE

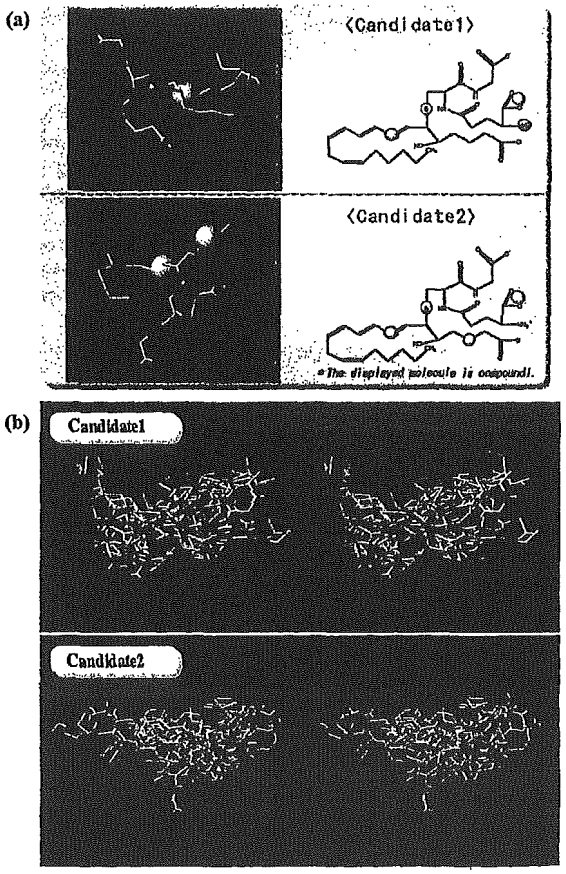

Fig. 4. (a) Property spheres common to compounds **1–9**. (b) Stereo views of superposed compounds in the training set (yellow molecule: compound **1**).

Table II. Results of CoMFA

Field type		Candidate 1		Candidate 2	
		ST + EL	ST + EL + C log P	ST + EL	ST + EL + C log P
Cross-validated	q^2	0.03	0.01	0.36	0.59
	s_{press}	1.21	1.15	0.80	0.64
No. of components		7	6	3	3
Conventional	r^2	1.00	1.00	0.99	0.99
	F	30122.14	2114.33	485.66	613.30
	s	0.01	0.03	0.09	0.08
Contribution (%)	ST	56.6	53.1	60.2	63.0
	EL	43.4	40.5	39.8	33.4
	C log P[a]	—	6.4	—	3.6

St, steric field; EL, electrostatic field; CoMFA, comparative molecular-field analysis.
[a] log P calculated by CLOGP.

program to determine the 3D pharmacophore of the ligand and to obtain the candidate binding conformations.

Selection of Candidate Binding Conformations

As shown in Table I, relatively stable conformers with molecular energies within 12 kcal/mol from the global minimum were selected as the conformers to be superposed. The cutoff value of 12 kcal/mol was confirmed in our previous study (19). For each ligand, the atomic groups that the property spheres were assigned to are shown in Figs. 1 (training set) and 2 (test set).

Initially, 3846 conformers of compound **1** and 15 conformers of compound **2** were superposed (Fig. 3). Each overlap was ranked on the basis of the SUPERPOSE score and the rmsd. As a result, we selected 30 conformers of compound **1** that represented good overlaps, with scores ranging between 14 and 15. Next, these 30 conformers of compound **1** and 234 conformers of compound **3** were superposed. As a result, we selected 16 conformers of compound **1** that showed good overlaps with conformers of compound **3**, with scores ranging between 16 and 17. The 16 selected conformers of compound **1** were then superposed to 798 conformers of compound **4**. No change was observed in the number of good overlaps at this stage, with scores ranging between 16 and 20 for all of the conformers. All 16 conformers of compound **1** were therefore superposed with 240 conformers of compound **5**. There were only two good overlaps for the superposition of compound **1** with compound **5**, with four commonly overlapped functional groups. Using the same method, the selected conformers of compound **1** were superposed to conformers of compounds **6–9** (Fig. 3). We finally obtained two conformers of compound **1** that were considered to be good candidates for the binding conformation. Figure 4a shows the common property spheres; namely, the pharmacophores obtained by superposition using compounds **1–9**.

Next, each candidate for the binding conformation was superposed to conformers of compounds **10–16** in the training set. The atomic groups that the ligand property spheres were assigned to are shown in Fig. 1. In this way, candidate binding conformations of compounds **10–16** were obtained. We then estimated the molecular alignment of ligand molecules (compounds **1–16**) that were essential to CoMFA (Fig. 4b). The

Table III. The Values of $\log(1/K_m)$ Calculated Using the Final CoMFA QSAR Model Compared with Experimental Data

	Experimental	Calculated	Residual
Compounds in the training set			
1 Leukotriene C4	6.60	6.70	−0.10
2 *p*-Nitrophenyl glucuronide	4.70	4.60	0.10
3 SN-38 glucuronide, lactone	5.64	5.63	0.01
4 SN-38 glucuronide, carboxylate	6.02	5.90	0.12
5 E3040 glucuronide	5.42	5.36	0.06
6 Leukotriene D4	5.82	5.77	0.05
7 *N*-acetyl leukotriene E4	5.28	5.33	−0.05
8 (*S*)-Grepafloxacin-glucuronide	5.00	5.00	0.00
9 (*R*)-Grepafloxacin-glucuronide	4.77	4.83	−0.06
10 L-Methotrexate	3.52	3.47	0.05
11 2,4-Dinitrophenyl-*S*-glutathione	4.68	4.76	−0.08
12 BQ-123	4.53	4.46	0.07
13 SN-38, carboxylate	4.16	4.25	−0.09
14 Temocaprilate	4.03	4.09	−0.06
15 5-Methyltetrahydrofolate	3.90	3.84	0.06
16 CPT-11, carboxylate	3.63	3.69	−0.06
Compounds in the test set			
A BQ-485	5.19	5.10	0.09
B MX-68	3.68	4.16	−0.48

two candidates of binding conformation of ligands for rat Mrp2 generated two types of molecular alignments, as shown in Fig. 4b. We also obtained binding conformation candidates for compounds **A–B** for the test set using a similar method to the training set. The test set was used to evaluate the predictive power of the CoMFA model obtained using the training set.

Determination of the Binding Conformation by CoMFA

CoMFA calculations were carried out using the two molecular alignments. The atomic charges of each conformer were calculated using MOPAC93 MNDO/ESP to evaluate the electrostatic field in CoMFA. Conventional CoMFA was performed with the QSAR option of SYBYL. For each molecular alignment (candidate 1 and candidate 2), two types of calculations were carried out together with an sp^3 carbon probe atom with a +1 charge: the first used steric and electrostatic fields, and the second used steric and electrostatic fields along with calculated values of log P (C log P). The CoMFA QSAR equations were calculated with the PLS algorithm. The optimal number of components in the final CoMFA PLS model was determined using the cross-validated R^2 (q^2) values obtained by the leave-one-out technique. The cross-validated R^2 (q^2) values, the standard error of the predictive sum of squares (s_{press}), and the standard error of the estimate (r^2) are listed in Table II for each candidate. The CoMFA PLS model with the highest q^2 values was assumed to best explain the binding conformation.

A good CoMFA model with three PLS components was obtained using the steric and electrostatic fields along with C log P for candidate 2. The final CoMFA model had a q^2 value of 0.59 with six PLS components, an s_{press} value of 0.64, an r^2 value of 0.99, and a standard error of 0.08. The experimental and calculated values of $\log(1/K_m)$ for each compound in the training set are listed in Table III. The property spheres shown in Fig. 5 illustrate the important atomic groups for the binding of each ligand molecule to rat Mrp2.

We also investigated the predictivity of the final CoMFA model using the test set of compounds. The values of $\log(1/K_m)$ calculated using the CoMFA model of candidate 2 with the steric field, electrostatic field, and C log P showed good agreement with the experimental values (Table III). We therefore concluded that the 3D structure of candidate 2 reflects the binding conformation of ligands for rat Mrp2. In the test set, the calculated value of $\log(1/K_m)$ for BQ-485 (5.10) compared well with the experimental value (5.19), whereas the calculated value of MX-68 contained a larger error (0.48). This might be the result of the difficulties of determining the atomic charges of MX-68, which has a pteridine ring, using MOPAC93 MNDO/ESP.

Figure 6a shows a contour map of the steric field from the final CoMFA model, together with the binding conformation of compound **1**: the green contours indicate areas in which bulky atomic groups are sterically favorable for the binding affinity, and the yellow contours indicate areas in which bulky groups are unfavorable for the binding affinity. Figure 6b shows a contour

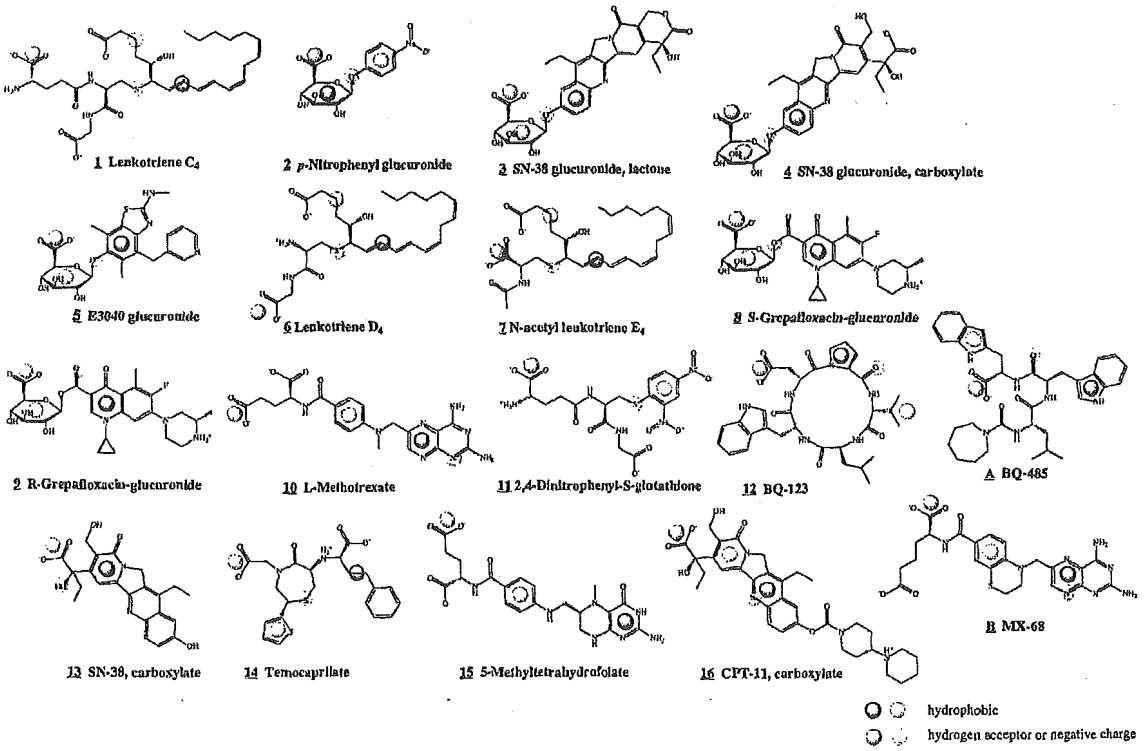

Fig. 5. Atomic groups involved in the binding of each ligand molecule to Mrp2/ABCC2.

(a) Steric field

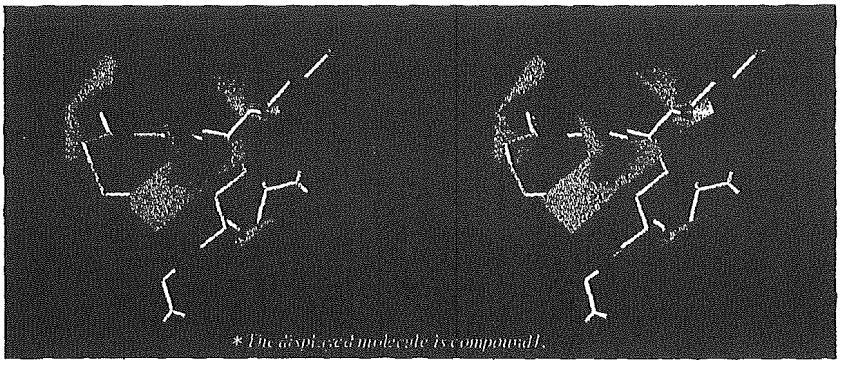

Green : Areas in which bulky atomic groups are sterically favorable for the binding affinity.

: Areas in which bulky groups are unfavorable for the binding affinity.

(b) Electrostatic field

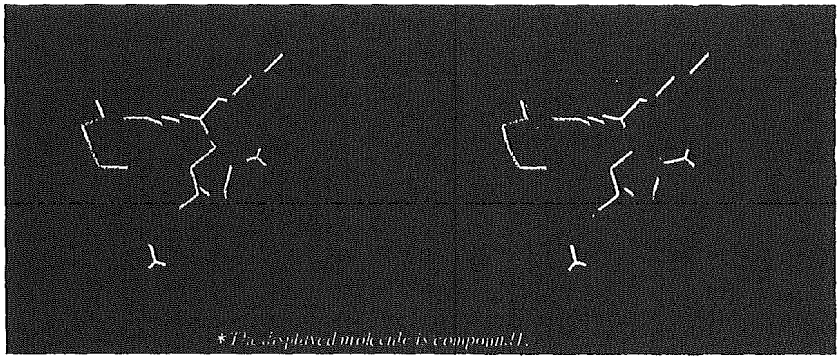

Blue : Areas in which atomic groups with positive charges are favorable for the binding affinity.

Red : Areas in which atomic groups with negative charges arefavorable for the binding affinity.

Fig. 6. Stereo views of contour maps obtained from the final CoMFA model. (a) Steric field. (b) Electrostatic field.

map of the electrostatic field from the final CoMFA model, together with the binding conformation of compound **1**: the blue contours indicate areas in which atomic groups with positive charges are advantageous to the binding of ligand with rat Mrp2, and the red contours show areas in which atomic groups with negative charges are favorable for the binding of ligand with rat Mrp2. The areas shown in the contour map are of great importance for explaining variation in the binding affinities of ligands with rat Mrp2.

DISCUSSION

Pharmacophore of Ligands for Rat Mrp2

We have identified a plausible binding conformation of ligands to rat Mrp2 by making full use of ligand-based drug design techniques. In this conformation, four property spheres that are common to all ligands were identified using the SUPERPOSE calculation. We propose that the spatial arrangement of the four functional groups expressed by these property spheres represents a 3D pharmacophore of ligands for rat Mrp2. Figure 7 shows a stereo view of these four property spheres along with the 3D structure of compound **1** and its structural formula. It appears that two hydrogen bond-acceptor groups (HA1 and HA2) and two hydrophobic groups (HP1 and HP2) are essential for the binding of ligands to rat Mrp2 and that these groups constitute the 3D pharmacophore. Figure 8 shows the relative distances between the four property spheres that represent the essential functional groups for ligand binding. The distances are as follows: HA1–HA2, ~5.0 &ARING;; HA1–HP1, ~5.3 &ARING;; HA1–

HP2, ~5.5 &ARING;; HA2–HP1, 4.7 &ARING;; HA2–HP2, 3.2 &ARING;; and HP1–HP2, 4.8 &ARING;.

Estimation of the Ligand-Binding Site of Rat Mrp2

A good CoMFA model was identified with the following parameters: a q^2 value of 0.59 with six PLS components, an s_{press} value of 0.64, an r^2 value of 0.99, and a standard error of 0.08. We suggest that the success of the CoMFA was a result of the use of the molecular alignment obtained using SUPERPOSE. This represents a unique and distinctive approach, in which the binding conformation and 3D pharmacophore of a ligand are estimated using ligand-based drug design techniques and are then applied to the molecular alignment, which is essential to CoMFA.

On the basis of the 3D pharmacophore and the contour map obtained from the CoMFA calculation, we have estimated the structure of the ligand-binding site of rat Mrp2 (Fig. 9). The four primary binding sites correspond to the 3D pharmacophore, comprising the four functional groups that are essential for the binding of ligands to rat Mrp2. The model also suggests that secondary binding sites, which correspond to specific contour levels in the CoMFA contour map, are important in explaining the variation of the binding affinities of ligands to rat Mrp2.

In conclusion, we propose that both hydrophobic and electrostatic interactions have vital roles in the binding of ligands to rat Mrp2. Ligand recognition seems to be achieved through interactions in the two hydrophobic sites and the two electrostatically positive sites (primary binding sites). Moreover, the broad substrate specificity of rat Mrp2 might be achieved by combinations of the secondary binding sites (two electrostatically positive sites and two electrostatically negative sites) with the primary binding sites.

The method described here for determining the binding conformation of ligands represents a powerful tool in cases where ligands have the same binding mode to the target protein. Of course, it should be noted that different binding modes might exist for some ligands; however, all of the ligands used in this analysis appeared to have the same binding mode, according to the results of the CoMFA. We believe that our data will be useful in the development of new com-

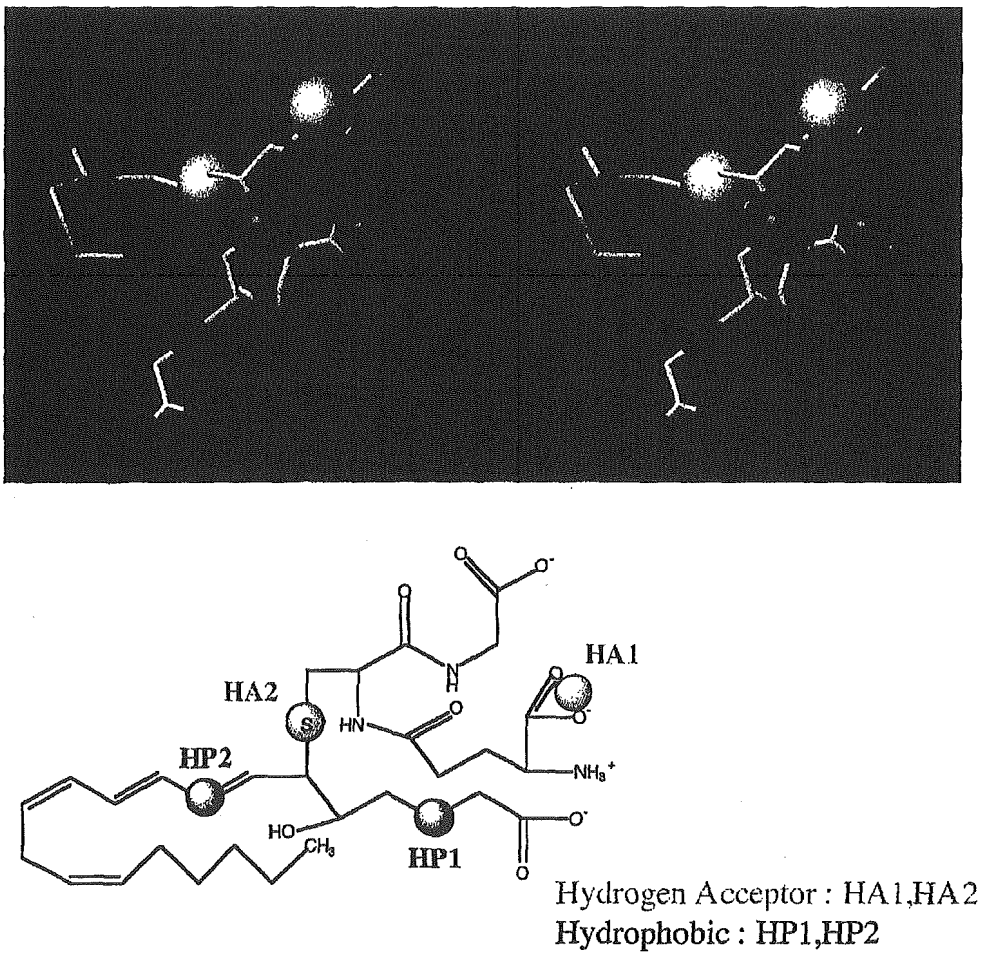

Fig. 7. A stereo view of the four property spheres that represent a 3D pharmacophore of ligands for Mrp2/ABCC2 and the 3D structure of compound 1 together with its structural formula.

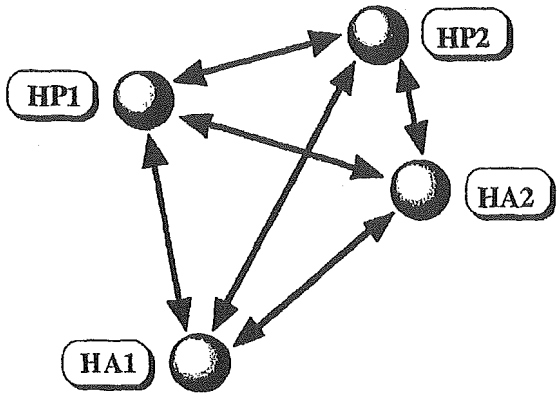

	Relative distances (Å)
HA1 - HA2	5.0 ± 0.9
HA1 - HP1	5.3 ± 0.7
HA1 - HP2	5.5 ± 1.6
HP1 - HA2	4.7 ± 0.8
HP1 - HP2	4.8 ± 1.1
HA2 - HP2	3.2 ± 1.2

Fig. 8. Relative distances between the four property spheres representing the functional groups that are essential for ligand binding.

compounds using the CoMFA QSAR model in order to evaluate their affinity for Mrp2.

REFERENCES

1. O. R. P. Elferink, D. K. Meijer, F. Kuipers, P. L. Jansen, A. K. Groen, and G. M. Groothuis. Hepatobiliary secretion of organic compounds; molecular mechanisms of membrane transport. *Biochim. Biophys. Acta* **1241**:215–268 (1995).
2. M. Yamazaki, H. Suzuki, and Y. Sugiyama. Recent advances in carrier-mediated hepatic uptake and biliary excretion of xenobiotics. *Pharm. Res.* **13**:497–513 (1996).
3. D. Keppler and J. Konig. Hepatic canalicular membrane 5: expression and localization of the conjugate export pump encoded by the *Mrp2* (*cMRP/cMOAT*) gene in liver. *FASEB J.* **11**:509–516 (1997).
4. K. Ito, H. Suzuki, T. Hirohashi, K. Kume, T. Shimizu, and Y. Sugiyama. Molecular cloning of canalicular multispecific organic anion transporter defective in EHBR. *Am. J. Physiol.* **272**:G16–G22 (1997).
5. C. C. Paulusma, P. J. Bosma, G. J. Zaman, C. T. Bakker, M. Otter, G. L. Scheffer, R. J. Scheper, P. Borst, and O. R. P. Elferink. Congenital jaundice in rats with a mutation in a multidrug resistance-associated protein gene. *Science* **271**:1126–1128 (1996).
6. K. Sathirakul, H. Suzuki, K. Yasuda, M. Hanano, O. Tagaya, T. Horie, and Y. Sugiyama. Kinetic analysis of hepatobiliary transport of organic anions in Eisai hyperbilirubinemic mutant rats. *J. Pharmacol. Exp. Ther.* **265**:1301–1312 (1993).
7. K. Sathirakul, H. Suzuki, T. Yamada, M. Hanano, and Y. Sugiyama. Multiple transport systems for organic anions across the bile canalicular membrane. *J. Pharmacol. Exp. Ther.* **268**:65–73 (1994).
8. M. Yamazaki, S. Akiyama, K. Ni'inuma, R. Nishigaki, and Y. Sugiyama. Biliary excretion of pravastatin in rats: contribution of the excretion pathway mediated by canalicular multispecific organic anion transporter. *Drug Metab. Dispos.* **25**:1123–1129 (1997).
9. H. Ishizuka, K. Konno, H. Naganuma, K. Sasahara, Y. Kawahara, K. Niinuma, H. Suzuki, and Y. Sugiyama. Temocaprilat, a novel angiotensin-converting enzyme inhibitor, is excreted in bile via an ATP-dependent active transporter (cMOAT) that is deficient in

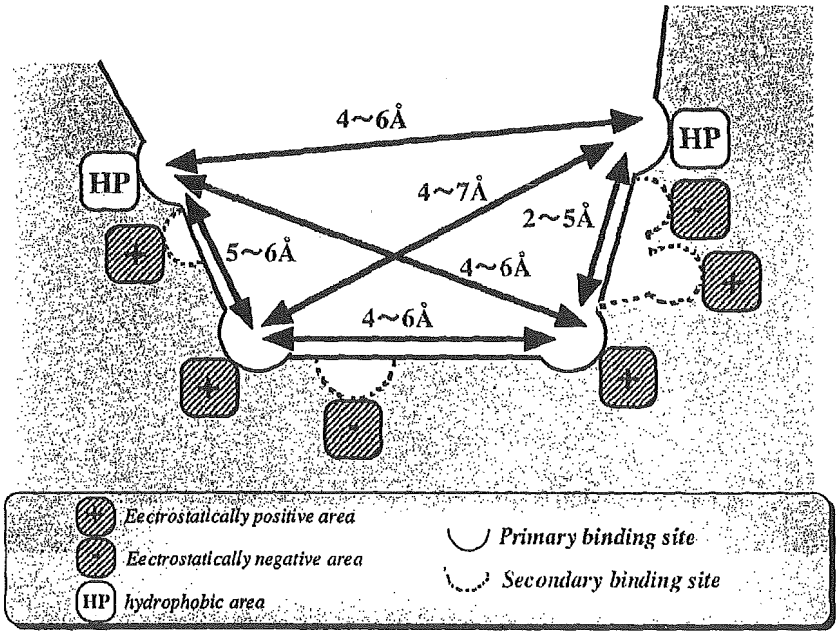

Fig. 9. Ligand-binding region of Mrp2/ABCC2 estimated using the 3D pharmacophore and CoMFA contour map.

Eisai hyperbilirubinemic mutant rats (EHBR). *J. Pharmacol. Exp. Ther.* **280**:1304–1311 (1997).
10. H. C. Shin, Y. Kato, T. Yamada, K. Niinuma, A. Hisaka, and Y. Sugiyama. Hepatobiliary transport mechanism for the cyclopentapeptide endothelin antagonist BQ-123. *Am. J. Physiol.* **272**: G979–G986 (1997).
11. T. Ishikawa, M. Muller, C. Klunemann, T. Schaub, and D. Keppler. ATP-dependent primary active transport of cysteinyl leukotrienes across liver canalicular membrane. Role of the ATP-dependent transport system for glutathione S-conjugates. *J. Biol. Chem.* **265**:19279–19286 (1990).
12. K. Kobayashi, Y. Sogame, H. Hara, and K. Hayashi. Mechanism of glutathione S-conjugate transport in canalicular and basolateral rat liver plasma membranes. *J. Biol. Chem.* **265**:7737–7741 (1990).
13. T. Nishida, Z. Gatmaitan, J. Roy-Chowdhry, and I. M. Arias. Two distinct mechanisms for bilirubin glucuronide transport by rat bile canalicular membrane vesicles. Demonstration of defective ATP-dependent transport in rats (TR-) with inherited conjugated hyperbilirubinemia. *J. Clin. Invest.* **90**:2130–2135 (1992).
14. O. Takenaka, T. Horie, K. Kobayashi, H. Suzuki, and Y. Sugiyama. Kinetic analysis of hepatobiliary transport for conjugated metabolites in the perfused liver of mutant rats (EHBR) with hereditary conjugated hyperbilirubinemia. *Pharm. Res.* **12**:1746–1755 (1995).
15. M. Trauner, M. Arrese, C. J. Soroka, M. Ananthanarayanan, T. A. Koeppel, S. F. Schlosser, F. J. Suchy, D. Keppler, and J. L. Boyer. The rat canalicular conjugate export pump (Mrp2) is down-regulated in intrahepatic and obstructive cholestasis. *Gastroenterology* **113**:255–264 (1997).
16. X. Y. Chu, Y. Kato, and Y. Sugiyama. Multiplicity of biliary excretion mechanisms for irinotecan, CPT-11, and its metabolites in rats. *Cancer Res.* **57**:1934–1938 (1997).
17. H. Suzuki and Y. Sugiyama. Role of transporters in the detoxification of xenobiotics: recent advances in the study of cMOAT/MRP. *Tanpakushitsu Kakusan Koso* **42**:1273–1284 (1997).
18. H. Tsujishita and S. Hirono. CAMDAS: an automated conformational analysis system using molecular dynamics. *J. Comput. Aided Mol. Des.* **11**:305–315 (1997).
19. K. Iwase and S. Hirono. Estimation of active conformations of drugs by a new molecular superposing procedure. *J. Comput. Aided Mol. Des.* **13**:499–512 (1999).
20. R. D. Cramer, D. E. Patterson, and J. D. Bunce. Comparative molecular field analysis (CoMFA). 1. Effect of shape on binding of steroids to carrier proteins. *J. Am. Chem. Soc.* **110**:5959–5967 (1988).
21. N. L. Allinger. Conformational analysis. 130. MM2. A hydrocarbon force field utilizing V1 and V2 torsional terms. *J. Am. Chem. Soc.* **99**:8127–8134 (1977).
22. H. Suzuki and Y. Sugiyama. Transporters for bile acids and organic anions. *Pharm. Biotechnol.* **12**:387–439 (1999).

THE JOURNAL OF BIOLOGICAL CHEMISTRY
Vol. 280, No. 2, Issue of January 14, pp. 1384–1391, 2005
Printed in U.S.A.

Use of Photoaffinity Labeling and Site-directed Mutagenesis for Identification of the Key Residue Responsible for Extraordinarily High Affinity Binding of UCN-01 in Human α1-Acid Glycoprotein*

Received for publication, September 27, 2004, and in revised form, October 26, 2004
Published, JBC Papers in Press, October 27, 2004, DOI 10.1074/jbc.M411076200

Masaaki Katsuki‡, Victor Tuan Giam Chuang‡§, Koji Nishi‡, Kohichi Kawahara¶, Hitoshi Nakayama¶, Noriyuki Yamaotsu‖, Shuichi Hirono‖, and Masaki Otagiri‡**

From the Departments of ‡Biopharmaceutics and ¶Molecular Cell Function, Graduate School of Medical and Pharmaceutical Sciences, Kumamoto University, 5-1 Oe-honmachi, Kumamoto, 862-0973, Japan, the §Department of Pharmacy, Faculty of Allied Health Sciences, Universiti Kebangsaan Malaysia, Jalan Raja Muda Abdul Aziz, 50300 Kuala Lumpur, Malaysia, and ‖The School of Pharmaceutical Sciences, Kitasato University, 5-9-1, Shirokane, Minato-ku, Tokyo, 108-8641, Japan

7-Hydroxystaurosporine (UCN-01) is a protein kinase inhibitor anticancer drug currently undergoing a phase II clinical trial. The low distribution volumes and systemic clearance of UCN-01 in human patients have been found to be caused in part by its extraordinarily high affinity binding to human α1-acid glycoprotein (hAGP). In the present study, we photolabeled hAGP with [^{3}H]UCN-01 without further chemical modification. The photolabeling specificity of [^{3}H]UCN-01 was confirmed by findings in which other hAGP binding ligands inhibited formation of covalent bonds between hAGP and [^{3}H]UCN-01. The amino acid sequence of the photolabeled peptide was concluded to be SDVVYTDXK, corresponding to residues Ser-153 to Lys-161 of hAGP. No PTH derivatives were detected at the 8th cycle, which corresponded to the 160th Trp residue. This strongly implies that Trp-160 was photolabeled by [^{3}H]UCN-01. Three recombinant hAGP mutants (W25A, W122A, and W160A) and wild-type recombinant hAGP were photolabeled by [^{3}H]UCN-01. Only mutant W160A showed a marked decrease in the extent of photoincorporation. These results strongly suggest that Trp-160 plays a prominent role in the high affinity binding of [^{3}H]UCN-01 to hAGP. A docking model of UCN-01 and hAGP around Trp-160 provided further details of the binding site topology.

Human α1-acid glycoprotein (hAGP)[1] is an acute phase protein with a molecular mass of 41 to 43 kDa and is heavily glycosylated (45%) (1). It contains sialic acids, which cause it to be negatively charged (pI = 2.7~3.2) (2). Its glycosylation pattern can change depending on the type of inflammation (3). The biological function of hAGP is not clear, although studies using *in vivo* models of inflammation indicate that it plays anti-inflammatory and immunomodulating roles and has protective effects (4, 5). The "basal" level of hAGP is ~20 μmol/liter, but hAGP levels can increase by 5–10-fold in response to stress, infection, or an inflammatory response to neoplasm (6, 7). In addition to increases in hAGP plasma concentration in certain cancers, changes in the expression of genetic variants of hAGP can occur according to the specific type of cancer (8). The levels of hAGP vary widely and heterogeneously among cancer patients; according to the type of disease, the composition of hAGP consists of various isoforms and degrees of glycosylation (9). Studies have shown that increases in circulating hAGP alter the pharmacokinetic disposition and pharmacological action of numerous drugs that bind to it (10–12). For example, increased hAGP levels associated with advanced tumors alter the pharmacokinetics of Imatinib (STI571), a tyrosine kinase inhibitor, in leukemia patients (13). hAGP also appears to be an independent predictor of response and a major objective prognostic factor of survival in patients with non-small cell lung cancer treated with docetaxel chemotherapy (14). Thus, hAGP is an important modulator of drug pharmacokinetics and pharmacodynamics in anticancer therapeutics.

7-Hydroxystaurosporine (UCN-01) has an indolocarbazole moiety and was originally isolated as a selective inhibitor of a Ca^{2+}- and phospholipid-dependent protein kinase (protein kinase C (PKC)) (15). UCN-01 is a derivative of staurosporine, which occurs naturally, inhibits numerous other kinases, and has greater selectivity for PKC than does staurosporine (16, 17). UCN-01 can mediate 3 distinct cellular effects *in vitro*: cell cycle arrest, induction of apoptosis, and potentiation of DNA damage-related toxicity (18–20). It exhibits anticancer activity against human and murine tumor cell lines that have aberrations in cellular signal transduction (21–24). Unlike other compounds with an indolocarbazole moiety, UCN-01 preferentially induces G_1 phase accumulation in various cell lines, and one of its mechanisms of action is clearly mediated by dephosphorylation of retinoblastoma protein and inhibition of cyclin-dependent kinase 2 (CDK2), an intracellular retinoblastoma protein kinase that regulates the transition from the G_1 to S phase (25). In addition, UCN-01 enhances the anticancer effects of several important chemotherapeutic drugs, including mitomycin C, cisplatin, and 5-fluorouracil, *in vitro* and *in vivo* (26–28). UCN-01 is currently in the phase II study of its effects on relapsed or refractory systemic anaplastic large cell and mature T-cell lymphomas (29, 30). UCN-01 was initially administered as a 72-h continuous infusion every 2 weeks, based on data from *in vitro* and xenograft preclinical models. However, in the first few patients, the drug had an unexpectedly long half-life (>30 days), which was 100 times longer than the

* The costs of publication of this article were defrayed in part by the payment of page charges. This article must therefore be hereby marked "*advertisement*" in accordance with 18 U.S.C. Section 1734 solely to indicate this fact.

** To whom correspondence should be addressed: Dept. of Biopharmaceutics, Graduate School of Pharmaceutical Sciences, Kumamoto University, 5-1 Oe-honmachi, Kumamoto, 862-0973, Japan. Tel.: 81-96-3714150; Fax: 81-96-3627690; E-mail: otagirim@gpo.kumamoto-u.ac.jp.

[1] The abbreviations used are: hAGP, human α1-acid glycoprotein; UCN-01, 7-hydroxystaurosporine; rhAGP, recombinant hAGP; PVDF, polyvinylidene difluoride; HPLC, high performance liquid chromatography; PKC, protein kinase C.

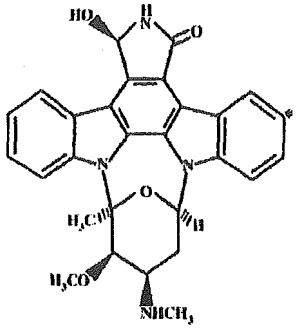

FIG. 1. **Chemical structure of [^{3}H]UCN-01.** *, ^{3}H-labeled position.

half-life observed in preclinical models. The distribution volumes (0.0796~0.158 liter/kg) and systemic clearance (0.0407~0.252 ml/h/kg) in the human patients were found to be extremely low. This pharmacokinetic behavior of UCN-01 in humans can partly be attributed to its specific high affinity binding to hAGP, which causes slow dissociation of UCN-01 from hAGP and thereby limits its disposition and elimination (31, 32). The binding constant for UCN-01 and hAGP, 8×10^8 M^{-1}, is the highest value ever reported for protein binding studies (33).

Several protein binding studies of hAGP had been conducted using a variety of techniques including equilibrium dialysis, ultrafiltration, chemical modification, and displacement (34–37). In a recent study, we identified the key factors contributing to the unusually high binding affinity between UCN-01 and hAGP: the substituent at C-7 of the UCN-01 molecule, and the Trp residues of hAGP (38). Crystallographic structural analysis has become more common and appears to be a good method for analysis of ligand-protein interaction, but there have been no reports of crystallographic structural analysis of hAGP. Certain experimental techniques allow direct evaluation of ligand-protein complexes, which can elucidate the binding chemistry of hAGP. Photoaffinity labeling is an essential complement to modeling and mutagenesis and allows direct, unambiguous identification of the contact region between a binding protein and its specific photoactivatable ligands (39–41). There is no photoaffinity labeling study that has led to the direct determination of labeled amino acid residues in hAGP. In the present study, we used [^{3}H]UCN-01 (Fig. 1) as a photoaffinity labeling agent to characterize the binding site of hAGP. Also, single residue mutants of recombinant hAGP (W25A, W122A, and W160A) were produced in order to determine which Trp was involved in the high affinity binding of [^{3}H]UCN-01. Finally, we constructed models of the docking of UCN-01 into the binding cavity, using a three-dimensional molecular model of hAGP.

EXPERIMENTAL PROCEDURES

Materials—[^{3}H]UCN-01 (12 Ci/mmol), UCN-01, UCN-02, and staurosporine were supplied by Kyowa Hakko Kogyo Co. (Shizuoka, Japan). hAGP (purified from cohn fraction VI) was purchased from Sigma. Sequencing grade modified trypsin was purchased from Promega. All other chemicals and solvents were of analytical grade. *N*-Glycosidase F recombinant (PNGase F) was purchased from Roche Applied Science. Plasma-derived AGP (pAGP), propranolol, and progesterone were purchased from Sigma. Potassium warfarin was donated by Eisai Co. (Tokyo, Japan). Restriction enzymes, *Escherichia coli* JM109, the DNA ligation kit, and the DNA polymerase Premix Taq® (EX Taq version) were obtained from Takara Biotechnology Co. Ltd. (Kyoto, Japan). The DNA sequencing kit was obtained from PerkinElmer Applied Biosystems (Tokyo, Japan). The Pichia expression kit was purchased from Invitrogen. DEAE Sephacel, phenyl-Sepharose Fast Flow, and Sephadex G-75 superfine were purchased from Amersham Biosciences.

Expression and Purification of Wild-type and Mutant rhAGP—Recombinant hAGP (rhAGP) was expressed in the methylotropic yeast *Pichia pastoris* using the expression vector pPIC9, and was purified by anionic exchange, hydrophobic interaction, and gel filtration chromatography (42). The single residue mutants W25A, W122A, and W160A were prepared using a QuikChange® XL site-directed mutagenesis kit, following the procedure of Braman *et al.* (43).

Purification of rhAGP—The growth medium was separated from the yeast by centrifugation (6000 × *g*, 10 min, 4 °C), and the secreted rhAGP was isolated from the medium as follows. The medium was brought to 60% saturation with ammonium sulfate at room temperature. The temperature was then lowered to 4 °C, and the pH was adjusted to 4.0. After shaking for 12 h, the precipitated protein was collected by centrifugation (12,000 × *g*, 60 min, 4 °C) and resuspended in distilled water. Dialysis was performed for 48 h at 4 °C against 100 volumes of distilled water, followed by a further 24 h of dialysis against 100 volumes of 10 mM Tris-HCl buffer (pH 7.4). Then, the solution was loaded onto a column of DEAE Sephacel. rhAGP was eluted with a linear gradient of 0–1 M NaCl in 10 mM Tris-HCl buffer (pH 7.4). The eluted rhAGP was loaded onto a column of phenyl-Sepharose Fast Flow. Finally, rhAGP was purified using Sephadex G-75 superfine resin.

Photoaffinity Labeling of hAGP—hAGP (50 μM) was incubated with [^{3}H]UCN-01 (0.08 μM) in 100 μl of 20 mM Tris-HCl (pH 7.4) in a 1.5-ml Eppendorf tube at room temperature in the dark for 60 min. The incubation mixture was then placed on ice and irradiated for 30 min by a 100-watt black light/blue lamp (310 nm, Ultra-Violet Products, Inc., San Gabriel, CA) at a distance of 10 cm. After irradiation, the photolabeled hAGP was precipitated by adding 1 ml of acetone, followed by centrifugation at 15 × 1000 rpm for 10 min. The pellet was washed with 1 ml of ethanol and centrifuged a second time.

SDS-PAGE and Electroblotting—Photolabeled hAGP was analyzed by SDS-PAGE using a 10% polyacrylamide gel (according to the method of Laemmli) and a sampling buffer (10 mM Tris-HCl, pH 7.6, 1% (w/v) SDS, 20 mM dithiothreitol, 4 mM EDTA, and 2% (w/v) sucrose). The concentration of protein was determined by Bradford assay using bovine serum albumin as the standard (44). After electrophoresis, the gel was electrophoretically transferred onto a PVDF membrane in a transfer buffer (25 mM Tris, 193 mM glycine, 10% methanol) using a semidry blotting assembly. The blotted membrane was stained with Coomassie Brilliant Blue R250, followed by complete drying in air.

Autoradiograpic Analysis—For autoradiographic analysis, the dried PVDF membrane was placed in contact with an imaging plate (BAS III, Fuji Photo Film Co.) in a cassette (BAS cassette 2040) at room temperature for 48 h. The imaging plate was scanned and analyzed using a Bio-Imaging Analyzer (model BAS FLA-3000 G; Fuji Photo Film Co.), and was then analyzed using L Process V1.6 software (Fuji Film Science Lab 98). The incorporation of radioactivity into individual fragments was quantified using Image Gauge V3.1 software (Fuji Film).

Competition Experiments—In order to determine the photolabeling specificity of the binding site of [^{3}H]UCN-01, hAGP (50 μM) was incubated with [^{3}H]UCN-01 (0.08 μM) in the presence of competitors (250 μM) prior to photolysis. The competitors were the UCN-01 analogues staurosporine and UCN-02, the basic drug propranolol, the acidic drug warfarin, and progesterone (representative steroid hormone). The photolabeled hAGP was separated by 10% gel SDS-PAGE and electroblotted onto a PVDF membrane before being subjected to autoradiographic analysis.

Reductive Pyridylethylation and Deglycosylation of hAGP—After the photolabeled hAGP was precipitated by acetone, 100 μl of the buffer was added to the precipitate. Then, 10 μl of 1% SDS and 1 M 2-mercaptoethanol were added to this solution, followed by reduction at 100 °C at 10 min. For deglycosylation of hAGP, 10 μl of 10% *n*-octanoyl-*N*-methylglucamide (MEGA-8), 50 μl of deionized water and 2 units of PNGase F were added to the reduction solution, and the resulting solution was incubated for 24 h. Then, 1 μl of 4-vinylpyridine was added, the mixture was further incubated in a N_2 atmosphere for 30 min at room temperature in the dark, and was then dialyzed for desalination.

Tryptic Digestion and Purification of Photolabeled hAGP Peptide Fragments—Tryptic digestion was performed in 50 mM NH_4HCO_3 (pH 7.8). After deglycosylation, deglycosylated hAGP was incubated with trypsin for 5 h at 37 °C. The ratio of trypsin to hAGP was 1:20 (w/w). Tryptic peptides were separated by reverse-phase C_{18} column (5 μm, 4.6 × 250 mm, Vydac) high performance liquid chromatography (HPLC) using an aqueous acetonitrile gradient in the presence of 0.1% trifluoroacetic acid. The separated peptides were fractionated every 30 s; 200 μl of each fraction were added to 2.5 ml of scintillation mixture; and the radioactivity was determined using a LSC-500 liquid scintillation counter (Aloka, Tokyo, Japan). The fraction with the highest radioactivity was collected in an Eppendorf tube, and was evaporated on a SpeedVac

evaporator until the volume of the sample was about 50 μl.

Capillary HPLC Separation and Sequencing—After evaporation, 10 μl of the sample was injected into an ABI 173 A MicroBlotter Capillary HPLC System (PerkinElmer Life Sciences) (45). The sample was manipulated according to the manufacturer's instructions (User's Manual, PerkinElmer Life Sciences). Meanwhile, the blotted membrane from the capillary HPLC separation using a C_{18} column (5 μm, 1.5 × 150 mm, PerkinElmer) was in contact with an imaging plate for 48 h prior to autoradiography analysis. The PVDF membrane was aligned with the chromatogram of a peptide map from the ABI 173 A MicroBlotter Capillary HPLC System. Portions of the PVDF membrane were excised for sequencing on an Applied Biosystems Procise Sequencer with reference to the autoradiogram.

Docking of UCN-01 to hAGP—The structure of hAGP has not previously been experimentally determined. As a model of the three-dimensional structure of hAGP for ligand docking, we used the modeled structure of hAGP obtained by Kopecky *et al.* (46). The initial structure of UCN-01 was taken from the crystal structure of the Chk1·UCN-01 complex (47, PDB ID 1NVQ). The docking calculation of UCN-01 to hAGP was performed using the SYBYL FlexX (48) under the condition that UCN-01 interacts with Trp-160. During the docking calculation, the structure of hAGP and the ring conformation of UCN-01 were kept rigid. The docking algorithm produced 158 different placements of UCN-01 in hAGP. All placements were evaluated by SYBYL CScore and were then ranked using AASS (Average of Auto-Scaled Scores), as follows in Equation 1.

$$AASS^{placement} = \left| \sum_i \frac{i\_Score^{placement} - \min(i\_Score)}{\max(i\_Score) - \min(i\_Score)} \right| \Big/ n \qquad \text{(Eq. 1)}$$

In the AASS calculation, $n = 5$ and i = F_Score (48), G_Score (49), PMF_Score (50), D_Score (51), ChemScore (52). Although the top 5 placements had nearly the same AASS values, they were classified into two types of binding modes. For each type, we chose the placement with the best AASS value as the candidate binding mode. In the type I model, UCN-01 is bound to a hydrophobic pocket formed by Val-41, Ile-44, Phe-48, and Val-156. In the type II model, UCN-01 is packed into a hydrophobic pocket consisting of Ile-28, Pro-131, Leu-138, Tyr-157, and Trp-160.

Refinement of Docking Models—To refine the docking models, the coordinates of the atoms of UCN-01 and the atoms of hAGP within 10 Å from UCN-01 were optimized to reduce the root mean square of the gradients of potential energy below 0.05 kcal mol^{-1} Å-1 using SYBYL 6.9.1 (Tripos, Inc., 2003). The Tripos force field was used for the molecular energy calculation. The AMBER 7 charges (53) were used as the atomic charges for hAGP. The Gasteiger-Hückel charges (54–57) were used as the charges for UCN-01. The cut-off distance for the non-bonded interactions was 10 Å. The distance-dependent dielectric constant of $4r$ was used. Due to the lack of hydrogen atoms in the modeled structure of hAGP, the initial positions of the hydrogen atoms in the hAGP were generated by the SYBYL.

Statistical Analysis—Statistical analysis of differences was performed by one-way ANOVA followed by the modified Fisher's least squares difference method.

RESULTS

Photolabeling of [^{3}H]UCN-01 to hAGP—The autoradiogram in Fig. 2 shows that the band of radiolabeled protein appeared only upon the photoirradiation of hAGP with [^{3}H]UCN-01. The radioactivity band indicated the incorporation of [^{3}H]UCN-01 to hAGP via photoirradiation. No band of radiolabeled protein could be observed for the sample without irradiation indicating that no covalent attachment of [^{3}H]UCN-01 to hAGP occurred in the dark. Exposure to light for 30 min was sufficient for the photoincorporation of [^{3}H]UCN-01 to hAGP (Fig. 3). The results indicate that [^{3}H]UCN-01 is photoactivatable and stable in the dark.

Competition Experiments—In a previous study using ultracentrifugation methods, it was concluded that the binding site for UCN-01 on hAGP partly overlaps with the binding site for basic drugs, acidic drugs, and steroid hormones (58). In the present photolabeling experiment, in order to determine the photolabeling specificity of [^{3}H]UCN-01, we used staurosporine and UCN-02 (a stereoisomer of UCN-01), which also bind

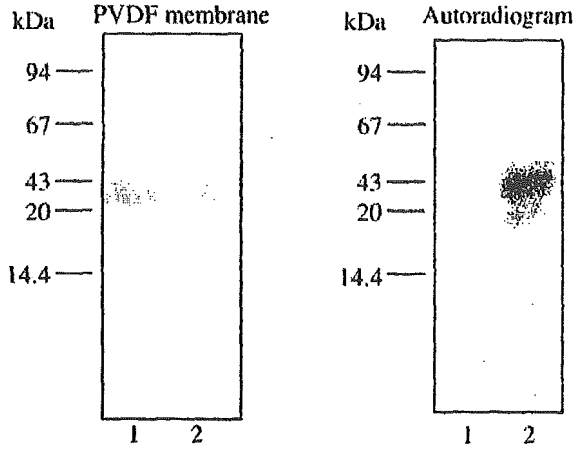

FIG. 2. **Photolabeling of hAGP with [^{3}H]UCN-01.** *Lane 1*, sample taken just prior to photoirradiation. *Lane 2*, sample taken after 30-min photoirradiation (>300 nm). 50 μM hAGP was incubated with 0.08 μM [^{3}H]UCN-01 for 60 min prior to photoirradiation. The samples were separated with 10% SDS-PAGE and electroblotted onto a PVDF membrane for autoradiographic analysis.

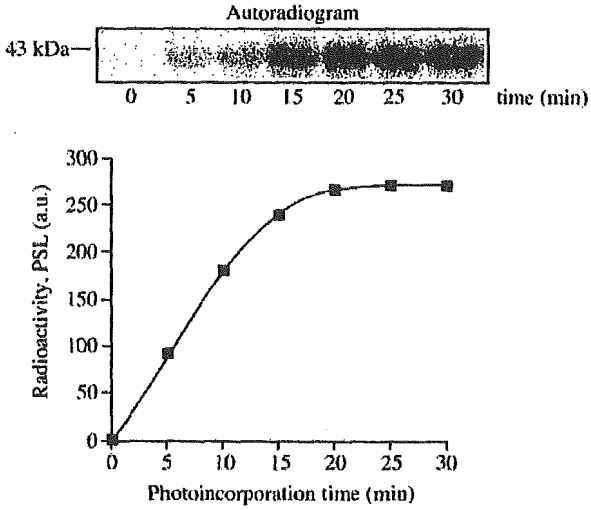

FIG. 3. **Time course of [^{3}H]UCN-01 photoincorporation.** 50 μM hAGP was incubated with 0.08 μM [^{3}H]UCN-01 for 60 min prior to photoirradiation. Aliquots of 100 μl were taken from the mixture solution at each time point as stated in the figure during irradiation until 30 min. All samples were separated with 10% SDS-PAGE and electroblotted onto a PVDF membrane for autoradiographic analysis. *PSL*, photostimulated luminescence.

hAGP, as competitors. All staurosporine analogs significantly inhibited photoincorporation, by more than 60% (Fig. 4). Other competitors that we used were representatives of other hAGP ligands: an acidic drug (warfarin), a basic drug (propranolol), and a steroid (progesterone). Warfarin and propranolol inhibited binding by less than 30%, but to a significant degree, whereas progesterone inhibited binding by about 60% (Table I).

Amino Acid Sequence of the Photolabeled Tryptic Peptides—Tryptic peptides of the hAGP photolabeled with [^{3}H]UCN-01 were separated by reverse phase HPLC using a C_{18} column. The major radioactive peptides were eluted in 10.5–11.5 min (Fig. 5, *A* and *B*). The fractions eluted within this time frame were collected and concentrated with a SpeedVac evaporator for further capillary HPLC analysis. The concentrated sample from previous HPLC analysis was separated and simulta-

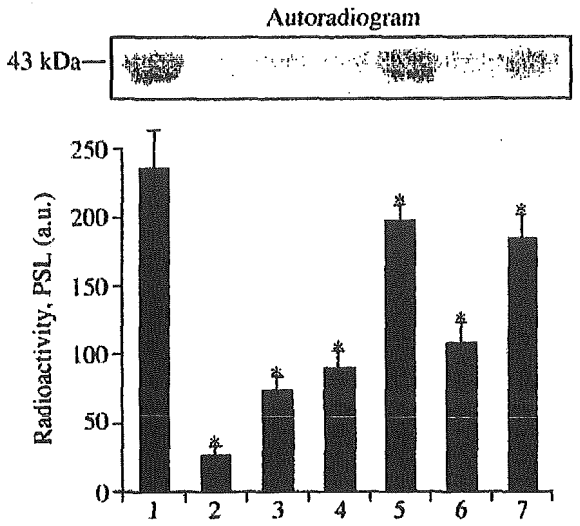

FIG. 4. **Photolabeling of hAGP with [^{3}H]UCN-01 in the presence of competitors.** *Lane 1*, no competitor; *lane 2*, cold UCN-01; *lane 3*, staurosporine; *lane 4*, UCN-02; *lane 5*, warfarin; *lane 6*, progesterone; *lane 7*, propranolol. 50 μM hAGP was incubated with 0.08 μM [^{3}H]UCN-01 and 250 μM competitors for 60 min prior to photoirradiation. The incubation mixture was irradiated for 30 min, separated with 10% SDS-PAGE, and electroblotted onto a PVDF membrane for autoradiographic analysis. *, statistically significant, compared with no competitor; $p < 0.01$. *PSL*, photostimulated luminescence.

TABLE I
Binding affinity constant and inhibition percentage by the competitors

Competitor	K_a	Inhibition
	M^{-1}	%
Cold UCN-01[a]	2.88×10^6	86.38
Staurosporine[a]	1.13×10^7	68.54
UCN-02[a]	1.48×10^6	61.52
Warfarin[b]	1.08×10^6	16.43
Progesterone[b]	1.00×10^5	58.71
Propranolol[b]	2.98×10^5	26.26

[a] Binding constant data taken from Ref. 38.
[b] Binding constant data taken from Ref 59.

neously blotted onto a strip of PVDF membrane using an ABI 173 A MicroBlotter Capillary HPLC System. Autoradiographic analysis of the PVDF membrane indicated that the radioactive spot corresponded to the peak observed at 84–85 min (Fig. 6, *A* and *B*). Edman sequencing of this spot revealed an amino acid sequence of SDVVYTDXK (Fig. 7), corresponding to Ser-153 to Lys-161 of hAGP.

Photolabeling of Wild-type and Mutant rhAGP with [^{3}H]UCN-01—Mutation of the 160th Trp residue of rhAGP to an Ala residue (W160A) caused a significant decrease in photoincorporation, by about 80%. In contrast, there was no significant difference in photoincorporation of [^{3}H]UCN-01 between wild-type rhAGP and the rhAGP mutants W25A and W122A (Fig. 8).

Docking of UCN-01 to hAGP—We constructed models of the docking of UCN-01 into the binding cavity of hAGP around Trp-160, using the three-dimensional molecular model of hAGP published by Kopecky *et al.* (46), to map the possible binding sites of hAGP. Molecular modeling calculations revealed 2 potential binding sites, type I and type II, around Trp-160, both of which were located in the outer region of hAGP (Fig. 9*A*). Table II shows the distance and nature of interaction between donors and acceptors in the models of types I and II. In the type II model, UCN-01 is packed into a surface cleft consisting of Ile-28, Pro-131, Glu-132, Lys-135, Leu-138, Tyr-157, Trp-160,

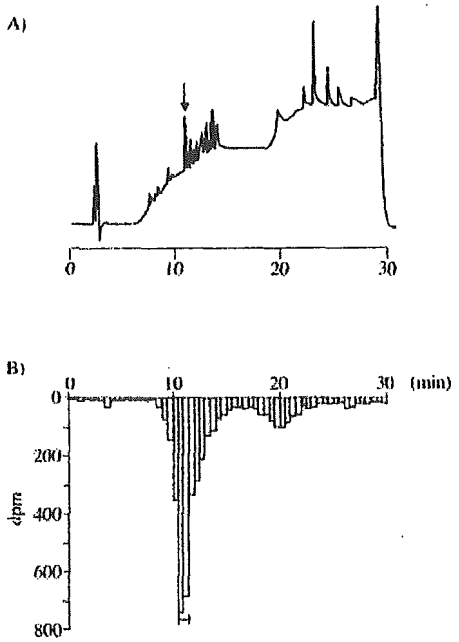

FIG. 5. **Reverse-phase HPLC separation of tryptic peptides of hAGP photolabeled with [^{3}H]UCN-01.** *A*, chromatogram of tryptic peptides of hAGP photolabeled with [^{3}H]UCN-01 detected at UV absorption wavelength of 210 nm. *B*, radioactivity of the reverse-phase fractions (200 μl) was determined by scintillation counting. An aliquot of 20 μl of the tryptic peptides was applied to a C_{18}-column and eluted at 1 ml/min using an aqueous acetonitrile gradient in the presence of 0.1% trifluoroacetic acid (from 5 to 95% acetonitrile over the course of 40 min).

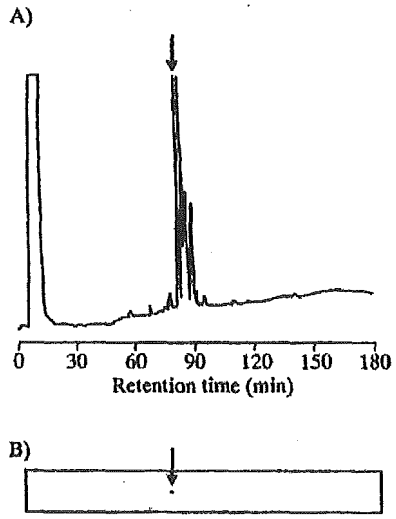

FIG. 6. **Chromatogram of capillary HPLC and autoradiogram of blotted PVDF membrane.** *A*, UV-absorption (210 nm). *B*, autoradiogram of blotted PVDF membrane. After purification of peptides using reverse-phase HPLC, an aliquot of 10 μl of the evaporating sample was applied to a C_{18} column and eluted at 5 μl/min using an aqueous acetonitrile gradient in the presence of 0.1% trifluoroacetic acid (from 5 to 95% acetonitrile over the course of 200 min). The blotted membrane from the capillary HPLC separation was in contact with an imaging plate for 48 h prior to autoradiography analysis.

and Lys-161 (Fig. 9*B*). The surrounding amino acid residues within 5 Å of the UCN-01 molecule include Lys-135, Tyr-157, Trp-160, and Lys-161. The oxygen atom in the sugar ring of

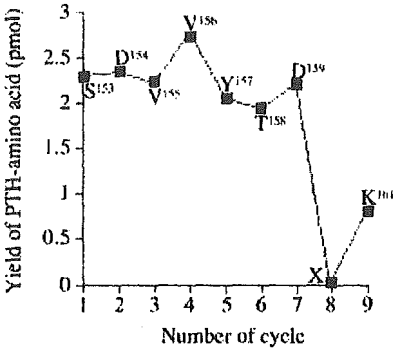

^{150}IPKSDVVYTDWKKDKC^{165}

FIG. 7. **N-terminal amino acid sequence analysis by the Edman degradation method and amino acid sequence of the photolabeled region of hAGP (tryptic peptides).** *PTH*, phenylthiohydantoin.

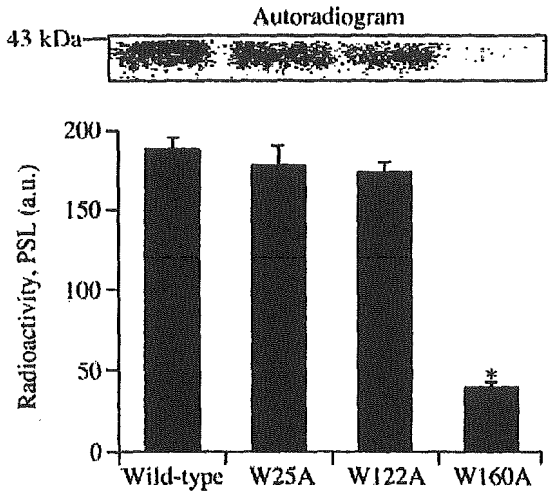

FIG. 8. **Photolabeling of wild type, W25A, W122A, and W160A with [^{3}H]UCN-01.** A sample of 50 μM rhAGP was incubated with 0.08 μM [^{3}H]UCN-01 for 60 min prior to photoirradiation. The samples were separated with 10% SDS-PAGE and electroblotted onto a PVDF membrane for autoradiographic analysis. *, statistically significant, compared with wild type; $p < 0.01$. *PSL*, photostimulated luminescence.

UCN-01 is in contact with Lys-135. The C=O group of UCN-01 was observed to form a hydrogen bond with the amino group of Trp-160, and electrostatic interaction was observed between the amino group of Lys-161 and both the 7-OH group and C=O group of UCN-01. Furthermore, the aromatic ring of UCN-01 is adjacent to Tyr-157 and Trp-160. In contrast, these interactions were not observed in the type I model, in which UCN-01 was shown to be packed into a surface cleft consisting of Val-41, Glu-43, Ile-44, Phe-48, Tyr-50, Val-156, Thr-158, and Trp-160 (data not shown).

DISCUSSION

The acute phase response alters the composition of carrier proteins in plasma, which may affect the blood deposition and transport of biomediators and drugs. Understanding the interaction of drugs with plasma proteins is essential to understanding their systemic pharmacology and toxicology. Thus, information about the effects of the acute phase response on the ligand binding ability of plasma can be used to optimize drug

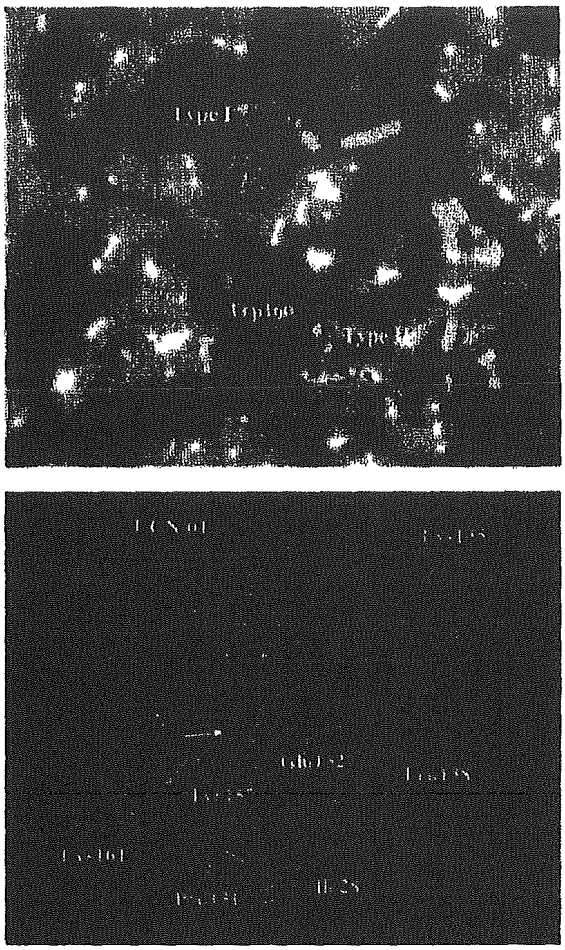

FIG. 9. *A*, type I and II docking models of UCN-01 and hAGP. Hydrophobic amino acids are shown in *green*. *B*, amino acid residues in a surface cleft around Trp-160 that interacts with UCN-01 exhibited in type II docking model. *Dotted line*, electrostatic interaction. *Arrow*, hydrogen bonding.

administration protocols in clinical practice. hAGP has been reported to be a major plasma protein that predominantly binds basic drugs (60). However, protein binding studies suggest that hAGP has 1 wide and flexible drug binding area that accommodates not only basic but also acidic and steroidal drugs (61). A current model of the hAGP binding site depicts a buried pocket with a negatively charged region that interacts with the N termini of basic drugs (62). The tertiary structure of hAGP has proven refractory to resolution, and structure-activity studies using various approaches are needed to clarify the nature of the binding site on this important protein.

The initial treatment protocol for UCN-01 was a 72-h infusion administered at 2-week intervals, because certain cell types (e.g. MDA-MB-468 breast carcinoma cells) required 72 h of drug exposure before irreversible growth inhibition occurred (23). However, the clinical outcome of the first 9 patients treated using this schedule demonstrated unexpectedly high concentrations of the drug with a long terminal elimination half-life ($t_{1/2}$). This led to a modification of the UCN-01 administration schedule, in which the recommended phase II dose of UCN-01 is administered as a 72-h continuous infusion at 42.5 mg/m^2/d over a 3-day period. Second and subsequent courses were administered for only 36 h at the same concentration and

TABLE II
Interaction and distance between donors and acceptors in the model of types I and II

Donor	Acceptor	Interaction	Distance
			Å
Type I			
UCN-01@NH_2	Glu-43@OE2	Hydrogen bonding	2.793
Tyr-50@OH	UCN-01@C=O	Hydrogen bonding	2.770
Type II			
Trp-160@NE1	UCN-01@C=O	Hydrogen bonding	2.878
Lys-135@NZ	UCN-01@-O-	Electrostatic	4.760
Lys-161@NZ	UCN-01@OH	Electrostatic	4.727
Lys-161@NZ	UCN-01@C=O	Electrostatic	4.350
Tyr-157	UCN-01	Stacking	4.204
Trp-160	UCN-01	Stacking	2.878

infusion rate, which effectively reduced the administered dose by 50% for the second and subsequent courses. In addition, the time between courses was increased from 2 weeks to 4 weeks (29). The extremely low clearance and small distribution volume of UCN-01 in humans may be partially caused by its high degree of binding to hAGP (32). Whereas many drugs that associate with hAGP have K_a values of 10^5–10^6 M^{-1}, UCN-01 is unique in its high affinity binding to hAGP, and has a K_a value of 8×10^8 M^{-1}. The results of this extraordinarily high binding affinity include a low volume of distribution (which approximates the extracellular volume) and long $t_{1/2}$ (32). The pharmacokinetic effects of the high affinity of UCN-01 for interaction with hAGP indicate that plasma levels of hAGP should be an important consideration in planning of clinical treatment. hAGP has been reported to be a major drug binding plasma protein that interacts mainly with basic drugs (63). Previous studies indicate that hAGP has 1 common drug binding site, which appears to be wide and flexible (61). Characterization of the binding site of UCN-01 on hAGP by Kurata *et al.* (58) revealed partial overlap with amino acid residues implicated in binding of basic drugs, acidic drugs, and steroid hormones. In a previous attempt to further characterize the binding site, we found that Trp-160 is particularly likely to play a major role in the binding of UCN-01. However, because that conclusion was the result of deducing the location of the 3 tryptophan residues, other experimental approaches are needed to confirm it. Currently, no x-ray crystallographic data is available for hAGP, which is a heterogeneous protein consisting of different isoforms and glycosylation states, that hinder crystallization. Therefore, in the present study, we examined the possibility of using UCN-01 as a photoaffinity-labeling agent. An ideal photolabeling reagent is stable not only in storage but also under the conditions in which the experiments are performed. Another problem with reagent stability is covalent attachment in the dark, either specific or nonspecific, to the protein under study. All the advantages of photoaffinity labeling are lost if such covalent attachment occurs. In the present study, a covalent bond was formed between UCN-01 and hAGP only upon photoirradiation (Fig. 2).

The results of the present examination of photoinhibition by staurosporine and UCN-02 were as expected (Table I). It is interesting that a change in the configuration of the hydroxyl group of UCN-01 or substitution of a hydrogen atom at the C-7 position of UCN-01 caused a decrease in binding inhibition effects. This confirms our finding that the substituent at C-7 of the UCN-01 molecule governs the affinity of its binding to hAGP. On the other hand, the extensive photoinhibition by progesterone, but not warfarin or propranolol, suggests that the binding site of staurosporine analogs overlaps to a greater extent with the binding site of steroids. This sharing of a binding region between UCN-01 and steroids is thought to be of minimal clinical significance, given the increased hAGP concentration in cancer and the extremely high binding affinity of UCN-01 for hAGP.

Sequence analysis of the major radioactive tryptic peptides separated from hAGP photolabeled with [^{3}H]UCN-01 showed that these peptides correspond to amino acids Ser-153 to Lys-161 of hAGP. In addition, no phenylthiohydantoin (PTH) derivatives were detected at the 8th cycle, which corresponds to the 160th Trp residue (Fig. 7), indicating that the covalent bond formed upon photolabeling of [^{3}H]UCN-01 to hAGP is relatively stable under the conditions of Edman degradation, and that it is highly likely that Trp-160 was photolabeled by [^{3}H]UCN-01.

All naturally occurring genetic variants of hAGP conserve the 3 Trp residues in the protein amino acid sequence: Trp-25, Trp-122, and Trp-160 (64). It is noteworthy that there is no significant difference in the binding percentage of UCN-01 between the F1*S and A variants of hAGP (38). 2 of 3 Trp residues of hAGP are relatively shielded from the bulk solvent, whereas the third Trp residue is located on the periphery of the domain. It has been deduced that Trp-25 is located deep in the binding pocket, and that Trp-122 is located in the central hydrophobic pocket of the protein (65). This suggests that Trp-160 is the Trp residue that is exposed to the bulk solvent. We also used site-directed mutagenesis to identify the key Trp residue involved in UCN-01 binding. Photolabeling of wild-type and mutant rhAGP with [^{3}H]UCN-01 revealed that photoincorporation was significantly lower for W160A than for the wild type. In contrast, the level of photoincorporation observed for the other 2 mutants, W25A and W122A, was comparable to that of the wild type. These results strongly support the hypothesis that Trp-160 is the key amino acid responsible for the extraordinarily high affinity of binding between UCN-01 and hAGP.

Previous studies have revealed the structures of UCN-01 and staurosporine bound to the active conformations of Chk1 (47), phospho-CDK2/cyclin A (66), and PDK1 (67). Coincidentally, as observed in the present study, the most important differences previously observed between staurosporine and UCN-01 complexes are the contacts involving the 7-OH group of UCN-01. Komander *et al.* (67) analyzed the relative affinities of staurosporine and UCN-01 for 29 different kinases, and found that binding that was potently inhibited by UCN-01 tended to involve molecules with a side chain that can directly form a hydrogen bond with the 7-OH group of UCN-01. Taking into account the experimental spectra and the unfavorable docking energy, Zsila *et al.* (68) suggested that it is unlikely that curcumin binds inside the central cavity of hAGP. The present docking models show that UCN-01 can interact with surface clefts of hAGP containing Trp-160. The interacting amino acid residues identified by the present type II model are consistent with results of our previous experimental studies of chemical modifications and protein binding (38), as well as those of

present studies using photoaffinity labeling and site-directed mutagenesis.

In order to further analyze the binding cleft of type II docking model, staurosporine and UCN-02, a stereoisomer of UCN-01 with an α-OH group at the C-7 position, were used to replace UCN-01 at the same position to produce another two docking models (data not shown). In general, all interacting amino acid residues in the two latter models were similar to those of the former, except that the α-OH group at the C-7 position of UCN-02 interacts with COOH group of Glu-132, in contrast to UCN-01 where the C-7 β-OH group interacts with Lys-161. On the other hand, no interaction of any form with the amino acid side chain could be observed for the substituent at C-7 position of staurosporine where hydrogen atom exists. Another amino acid residue that deserved attention was Lys-135 as its distance from the sugar ring of UCN-02 was more than 5 Å, the greatest among the three models.

The following sequence of binding affinity for hAGP has previously been observed: UCN-01 > staurosporine > UCN-02 (38). The aromatic ring of UCN-01 is stacked on Trp-160, and the hydrophobic interaction is strengthened by the electrostatic interaction between the 7-OH group of UCN-01 and Lys-161, which are located on the same side of Trp-160. In contrast, the hydrogen bond between the 7-OH group of UCN-02 and Glu-132, which is located on the opposite side, appears to weaken the hydrophobic interaction, because the ring of UCN-02 has been diverted away from Trp-160. The aromatic ring of staurosporine is not diverted from Trp-160, due to the absence of the 7-OH group. In order to gain deeper insight on the binding mechanism of UCN-01 to hAGP, experiments using Glu-132 and Lys-161 hAGP mutants to examine the role of each mutated amino acid residue in the high affinity binding of UCN-01 is currently underway in our laboratory.

Staurosporine is a natural product derived from fermentation extracts of several bacterial species. Staurosporine was initially identified as a potent inhibitor of PKC, which is a Ca^{2+}- and phospholipid-activated kinase (69). Different isoforms of PKC are activated in response to growth factors that act on receptor tyrosine kinases and 7-transmembrane domain receptors (70). Studies have revealed that staurosporine is a broad-acting kinase inhibitor with little specificity or selectivity for PKC (71). Recently, the staurosporine analog *N*-benzoylstaurosporine (PKC412) has been reported to exhibit strong hAGP binding, and to have unusual pharmacokinetics similar to those of staurosporine, which were not predicted by animal studies (72). PKC412 is the only staurosporine inhibitor of protein kinases other than UCN-01 that has been subjected to a clinical trial. There has been a study of oral administration of PKC412 once daily (73). It is interesting that PKC412 exhibits complex pharmacology resulting from binding to hAGP. Preclinical experiments had shown extensive binding of PKC412 to human plasma proteins, with ~88–98% protein binding, depending on the drug concentration (72). Rates of binding of PKC412 to hAGP were particularly interesting. In the preclinical experiments, the plasma concentrations of PKC412 were higher, and the half-life was longer than predicted from animal studies and single dose kinetics studies with healthy volunteers (72). In contrast to UCN-01, PKC412 was metabolized to 7-hydroxy-PKC412 and an *O*-demethyl-PKC412, both of which also bound to hAGP. The major metabolite had a particularly long half-life (74). It is possible that PKC412 and its metabolite preferentially bind to hAGP *in vivo*, and this may account for the longer than anticipated plasma half-life. The dynamics of dissociation of PKC412 from plasma proteins and tissue distribution of PKC412 are likely to be complex, and plasma levels may not accurately reflect drug concentration in target tissues. Because plasma pharmacokinetic evaluation is complicated by protein binding and metabolism, studies using biologic markers of PKC inhibition can contribute to optimization of PKC412 administration.

CONCLUSIONS

Because of the potential implications of species-specific binding of UCN-01 to hAGP in human plasma for the development of staurosporine analogs, studies of analogs of UCN-01 and of PKC412, which lack hAGP binding or very weakly bind to hAGP, should be conducted along with studies of the potential usefulness of staurosporine pharmacophores. Characterization of the binding site of UCN-01 on hAGP using photoaffinity labeling and site-directed mutagenesis techniques has provided direct evidence that strongly indicates that Trp-160 plays an important role in the binding interaction between UCN-01 and hAGP. In addition to the obvious pharmacokinetic implications of the extraordinarily high affinity of binding of UCN-01 to hAGP, the present results suggest that hAGP is a suitable platform for further design of novel staurosporine analog anticancer drugs, and also for evaluation of side effects and drug interaction in clinical settings. The present results provide clues to the design of future second-generation therapeutic agents, and can serve as a basis for future studies of UCN-01 administered alone and in combination with other anticancer drugs, particularly DNA-damaging agents.

Acknowledgment—We thank Dr. Vladimir Kopecky, Jr. of the Institute of Physics, Charles University in Prague, for providing us with the protein moiety of hAGP in the native state and with docked progesterone in a PDB format.

REFERENCES

1. Schmid, K., Nimerg, R. B., Kimura, A., Yamaguchi, H., and Binette, J. P. (1977) *Biochim. Biophys. Acta* **492**, 291–302
2. Kremer, J. M., Wilting, J., and Janssen, L. H. (1988) *Pharmacol. Rev.* **40**, 1–47
3. Van Dijk, W. (1995) *Adv. Exp. Med. Biol.* **376**, 223–229
4. Hochepied, T., Berger, F. G., Baumann, H., and Libert, C. (2003) *Cytokine Growth Factor Rev.* **14**, 25–34
5. Cheresh, D. A., Haynes, D. H., and Distasio, J. A. (1984) *Immunology* **51**, 541–548
6. Morita, K., and Yamaji, A. (1995) *Ther. Drug Monit.* **17**, 107–112
7. Mackiewicz, A., and Mackiewicz, K. (1995) *Glycoconj. J.* **12**, 241–247
8. Duche, J. C., Urien, S., Simon, N., Malaurie, E., Monnet, I., and Barre, J. (2000) *Clin. Biochem.* **33**, 197–202
9. Fan, C., Stendahl, U., Stjernberg, N., and Beckman, L. (1995) *Oncology* **52**, 498–500
10. Mazoit, J. X., and Dalens, B. J. (2004) *Clin. Pharmacokinet.* **43**, 17–32
11. Veering, B. T., Burm, A. G., Feyen, H. M., Olieman, W. M., Souverijn, J. H., and Van Kleef, J. W. (2002) *Anesthesiology* **96**, 1062–1069
12. Hedaya, M. A., and Daoud, S. S. (2001) *Anticancer Res.* **21**, 4005–4010
13. Gambacorti-Passerini, C., Zucchetti, M., Russo, D., Frapolli, R., Verga, M., Bungaro, S., Tornaghi, L., Rossi, F., Pioltelli, P., Pogliani, E., Alberti, D., Corneo, G., and D'Incalci, M. (2003) *Clin. Cancer Res.* **9**, 625–632
14. Bruno, R., Olivares, R., Berille, J., Chaikin, P., Vivier, N., Hammershaimb, L., Rhodes, G. R., and Rigas, J. R. (2003) *Clin. Cancer Res.* **9**, 1077–1082
15. Takahashi, I., Kobayashi, E., Asano, K., Yoshida, M., and Nakano, H. (1987) *J Antibiot (Tokyo)* **40**, 1782–1784
16. Penuelas, S., Alemany, C., Noe, V., and Ciudad, C. J. (2003) *Eur. J. Biochem.* **270**, 4809–4822
17. Yu, Q., La, Rose, J., Zhang, H., Takemura, H., Kohn, K. W., and Pommier, Y. (2002) *Cancer Res.* **62**, 5743–5748
18. Facchinetti, M. M., De, Siervi, A., Toskos, D., and Senderowicz, A. M. (2004) *Cancer Res.* **64**, 3629–3637
19. Dai, Y., Pei, X. Y., Rahmani, M., Conrad, D. H., Dent, P., and Grant, S. (2004) *Blood* **103**, 2761–2770
20. Tenzer, A., and Pruschy, M. (2003) *Curr. Med. Chem. Anti-Cancer Agents* **3**, 35–46
21. Akinaga, S., Gomi, K., Morimoto, M., Tamaoki, T., and Okabe, M. (1991) *Cancer Res.* **51**, 4888–4892
22. Akinaga, S., Nomura, K., Gomi, K., and Okabe, M. (1994) *Cancer Chemother. Pharmacol.* **33**, 273–280
23. Seymaeve, C. M., Stetler-Stevenson, M., Sebers, S., Kaur, G., Sausville, E. A., and Worland, P. J. (1993) *Cancer Res.* **53**, 2081–2086
24. Senderowicz, A. M. (2003) *Oncogene* **22**, 6609–6620
25. Akiyama, T., Yoshida, T., Tsujita, T., Shimizu, M., Mizukami, T., Okabe, M., and Akinaga, S. (1997) *Cancer Res.* **57**, 1495–1501
26. Akinaga, S., Nomura, K., Gomi, K., and Okabe, M. (1993) *Cancer Chemother. Pharmacol.* **32**, 183–189
27. Abe, S., Kubota, T., Otani, Y., Furukawa, T., Watanabe, M., Kumai, K., and Kitajima, M. (2000) *Jpn. J. Cancer Res.* **91**, 1192–1198
28. Bunch, R. T., and Eastman, A. (1996) *Clin. Cancer Res.* **2**, 791–797

29. Sausville, E. A., Arbuck, S. G., Messmann, R., Headlee, D., Bauer, K. S., Lush, R. M., Murgo, A., Figg, W. D., Lahusen, T., Jaken, S., Jing, X., Roberge, M., Fuse, E., Kuwabara, T., and Senderowicz, A. M. (2001) *J. Clin. Oncol.* **19,** 2319–2333
30. Senderowicz, A. M. (2002) *Hematol. Oncol. Clin. North Am.* **16,** 1229–1253
31. Fuse, E., Tanii, H., Takai, K., Asanome, K., Kurata, N., Kobayashi, H., Kuwabara, T., Kobayashi, S., and Sugiyama, Y. (1999) *Cancer Res.* **59,** 1054–1060
32. Fuse, E., Tanii, H., Kurata, N., Kobayashi, H., Shimada, Y., Tamura, T., Sasaki, Y., Tanigawara, Y., Lush, R. D., Headlee, D., Figg, W. D., Arbuck, S. G., Senderowicz, A. M., Sausville, E. A., Akinaga, S., Kuwabara, T., and Kobayashi, S. (1998) *Cancer Res.* **58,** 3248–3253
33. Sausville, E. A., Lush, R. D., Headlee, D., Smith, A. C., Figg, W. D., Arbuck, S. G., Senderowicz, A. M., Fuse, E., Tanii, H., Kuwabara, T., and Kobayashi, S. (1998) *Cancer Chemother. Pharmacol.* **42,** 54–59
34. Bailey, D. N., and Briggs, J. R. (2004) *Ther. Drug Monit.* **26,** 40–43
35. Nakai, D., Kumamoto, K., Sakikawa, C., Kusaka, T., and Tokui, T. (2004) *J. Pharm. Sci.* **93,** 847–854
36. Kute, T., and Westphal, U. (1976) *Biochim. Biophys. Acta* **420,** 195–213
37. Haughey, D. B., Steinberg, I., and Lee, M. H. (1985) *J. Pharm. Pharmacol.* **37,** 285–288
38. Katsuki, M., Chuang, V. T. G., Nishi, K., Suenaga, A., and Otagiri, M. (2004) *Pharm. Res.* **21,** 1648–1655
39. Hatanaka, Y., and Sadakane, Y. (2002) *Curr. Top Med. Chem.* **2,** 271–288
40. Chang, S. H., and Low, P. S. (2003) *J. Biol. Chem.* **278,** 6879–6884
41. Sato, T., Shimada, Y., Nagasawa, N., Nakanishi, S., and Jingami, H. (2003) *J. Biol. Chem.* **278,** 4314–4321
42. Nishi, K., Fukunaga, N., and Otagiri, M. (2004) *Drug Metab. Dispos.* **32,** 1069–1074
43. Braman, J., Papworth, C., and Greener, A. (1996) *Methods Mol. Biol.* **57,** 31–44
44. Zor, T., and Selinger, Z. (1996) *Anal. Biochem.* **236,** 302–308
45. Davis, M. T., and Lee, T. D. (1992) *Protein Sci.* **1,** 935–944
46. Kopecky, V., Jr., Ettrich, R., Hofbauerova, K., and Baumruk, V. (2003) *Biochem. Biophys. Res. Commun.* **300,** 41–46
47. Zhao, B., Bower, M. J., McDevitt, P. J., Zhao, H., Davis, S. T., Johanson, K. O., Green, S. M., Concha, N. O., and Zhou, B. B. (2002) *J. Biol. Chem.* **277,** 46609–46615
48. Rarey, M., Kramer, B., Lengauer, T., and Klebe, G. (1996) *J. Mol. Biol.* **261,** 470–489
49. Jones, G., Willett, P., Glen, R. C., Leach, A. R., and Taylor, R. (1997) *J. Mol. Biol.* **267,** 727–748
50. Muegge, I., and Martin, Y. C. (1999) *J. Med. Chem.* **42,** 791–804
51. Kuntz, I. D., Blaney, J. M., Oatley, S. J., Langridge, R., and Ferrin, T. E. (1982) *J. Mol. Biol.* **161,** 269–288
52. Eldridge, M. D., Murray, C. W., Auton, T. R., Paolini, G. V., and Mee, R. P. (1997) *J. Comput-Aided Mol. Design* **11,** 425–445
53. Cornell, W. D., Cieplak, P., Bayly, C. I., Gould, I. R., Merz, K. M., Jr., Ferguson, D. M., Spellmeyer, D. C., Fox, T., Caldwell, J. W., and Kollman, P. A. (1995) *J. Am. Chem. Soc.* **117,** 5179–5197
54. Gastoiger, J., and Marsili, M. (1980) *Tetrahedron* **36,** 3219–3228
55. Gasteiger, J., and Marsili, M. (1981) *Organ. Magn. Reson.* **15,** 353–360
56. Marsili, M., and Gasteiger, J. (1980) *Croat. Chem. Acta* **53,** 601–614
57. Purcell, W. P., and Singer, J. A. (1967) *J. Chem. Eng. Data* **12,** 235–246
58. Kurata, N., Matsushita, S., Nishi, K., Watanabe, H., Kobayashi, S., Suenaga, A., and Otagiri, M. (2000) *Biol. Pharm. Bull.* **23,** 893–895
59. Urien, S., Giroud, Y., Tsai, R. S., Carrupt, P. A., Bree, F., Testa, B., and Tillement, J. P. (1995) *Biochem. J.* **306,** 545–549
60. Israili, Z. H., and Dayton, P. G. (2001) *Drug Metab. Rev.* **33,** 161–235
61. Miyoshi, T., Yamamichi, R., Maruyama, T., Takadate, A., and Otagiri, M. (1992) *Biochem. Pharmacol.* **43,** 2161–2167
62. Taheri, S., Cogswell, L. P., 3rd., Gent, A., and Strichartz, G. R. (2003) *J. Pharmacol. Exp. Ther.* **304,** 71–80
63. Routledge, P. A. (1986) *Br. J. Clin. Pharmacol.* **22,** 499–506
64. Deute, L., Pizza, M. G., Metspalu, A., and Cortese, R. (1987) *EMBO J.* **6,** 2289–2296
65. Friedman, M. L., Schlueter, K. T., Kirley, T. L., and Halsall, H. B. (1985) *Biochem. J.* **232,** 863–867
66. Johnson, L. N., De Moliner, E., Brown, N. R., Song, H., Barford, D., Endicott, J. A., and Noble, M. E. (2002) *Pharmacol. Ther.* **93,** 113–124
67. Komander, D., Kular, G. S., Bain, J., Elliott, M., Alessi, D. R., and Van Aalten, D. M. (2003) *Biochem. J.* **375,** 255–262
68. Zsila, F., Bikadi, Z., and Simonyi, M. (2004) *Bioorg. Med. Chem.* **12,** 3239–3245
69. Tamaoki, T., Nomoto, H., Takahashi, I., Kato, Y., Morimoto, M., and Tomita, F. (1986) *Biochem. Biophys. Res. Commun.* **135,** 397–402
70. Rodriguez-Fernandez, J. L., and Rozengurt, E. (1998) *J. Biol. Chem.* **273,** 19321–19328
71. Katira, A., Knox, K. A., Finney, M., Michell, R. H., Wakelam, M., and Gordon, J. (1993) *Clin. Exp. Immunol.* **92,** 347–352
72. Propper, D. J., McDonald, A. C., Man, A., Thavasu, P., Balkwill, F., Braybrooke, J. P., Caponigro, F., Graf, P., Dutreix, C., Blackie, R., Kaye, S. B., Ganesan, T. S., Talbot, D. C., Harris, A. L., and Twelves, C. (2001) *J. Clin. Oncol.* **19,** 1485–1492
73. Monnerat, C., Henriksson, R., Le, Chevalier, T., Novello, S., Berthaud, P., Paivre, S., and Raymond, E. (2004) *Ann. Oncol.* **15,** 316–323
74. Eder, J. P., Jr., Garcia-Carbonero, R., Clark, J. W., Supko, J. G., Puchalski, T. A., Ryan, D. P., Deluca, P., Wozniak, A., Campbell, A., Rothermel, J., and LoRusso, P. (2004) *Investig. New Drugs* **22,** 139–150

New AMBER Force Field Parameters of Heme Iron for Cytochrome P450s Determined by Quantum Chemical Calculations of Simplified Models

AKIFUMI ODA,[1] NORIYUKI YAMAOTSU,[2] SHUICHI HIRONO[2]
[1]*Discovery Laboratories, Toyama Chemical Co., Ltd., 2-4-1 Shimookui, Toyama 930-8508, Japan*
[2]*School of Pharmaceutical Sciences, Kitasato University, 5-9-1 Shirokane, Minato-ku, Tokyo 108-8641, Japan*

Received 24 September 2004; Accepted 20 December 2004
DOI 10.1002/jcc.20221
Published online 6 April 2005 in Wiley InterScience (www.interscience.wiley.com).

Abstract: The heme protein, cytochrome P450, is an oxidoreductase that plays an important role in drug metabolism. To model P450s using molecular mechanics methods and classical molecular dynamics simulations, force field parameters and atomic charges are required. Because these parameters are generally obtained by quantum chemical methods, an appropriate simplified model for the iron–porphyrin system was needed. In this study, two models with a five-coordinated Fe(III) mimicking the sextet spin state of P450s are proposed, which are optimized by semiempirical and *ab initio* unrestricted Hartree–Fock methods. The results produced using the simpler of the two models were similar to those of the more complex model; therefore, the more simplified model of P450 can be used without a loss of accuracy. Furthermore, several quantum chemical calculations were carried out on the simpler model to investigate which method was most suitable for iron–porphyrin systems. The results calculated by hybrid density functional theory (DFT), with the MIDI basis set for iron, reproduced the three-dimensional structures determined by X-ray diffraction and extended X-ray absorption fine-structure experiments. From these results, atomic charges and force-field parameters for molecular mechanics and molecular dynamics calculations were obtained.

 J Comput Chem 26: 818–826, 2005

Key words: AMBER force-field; atomic charge; cytochrome P450; DFT; iron–porphyrin

Introduction

Cytochrome P450 is a family of oxidoreductases with a wide variety of substrates, and is among the most important enzymes for metabolism within the living body. P450s metabolize both endogenous and exogenous substrates. Steroids,[1] arachidonic acid,[2,3] and retinoid[4,5] are all reported to be endogenous substrates of these enzymes. Metabolites from these substrates have important biological functions; therefore, P450 proteins play a significant role in maintaining the homeostasis of the living body. They also metabolize exogenous substrates, such as drugs and toxic agents, and are responsible for the metabolic activation of exogenous mutagenic compounds. Around 20 P450s have been reported to play important roles in drug metabolism in humans[6] and to metabolize a variety of different drugs.[7] Polymorphisms in some important P450s, for example, CYP2C9, CYP2C19, and CYP2D6, are responsible for differing drug metabolism between individuals.[8] Therefore, investigating whether a specific drug inhibits and/or is metabolized by P450s is desirable in drug design studies.

P450s are monooxygenases that include a heme moiety axially ligated to a cysteinyl (CYS) sulfur. Catalytic reactions occur at the iron center of heme, and P450s generally insert an oxygen atom into hydrophobic molecules between the carbon and hydrogen atoms of a C—H bond or the two carbon atoms of a C—C bond. The catalytic cycle of P450s is illustrated in Figure 1. The oxidation state of the heme iron (Fe(II) or Fe(III)), the spin state (high- or low-spin) and the number of ligands (five- or six-coordinated) all play important roles in this cycle.[9] In the first step, the heme iron is low-spin six-coordinated Fe(III). A water molecule is at the coordination position trans to the CYS. Upon substrate docking, the water ligand is unbound from the iron atom. Substrate binding

Correspondence to: A. Oda; e-mail: AKIFUMI_ODA@toyama-chemical.co.jp

This article includes Supplementary Material available from the authors upon request or via the internet at http://www.interscience.wiley.com/jpages/0192-8651/suppmat

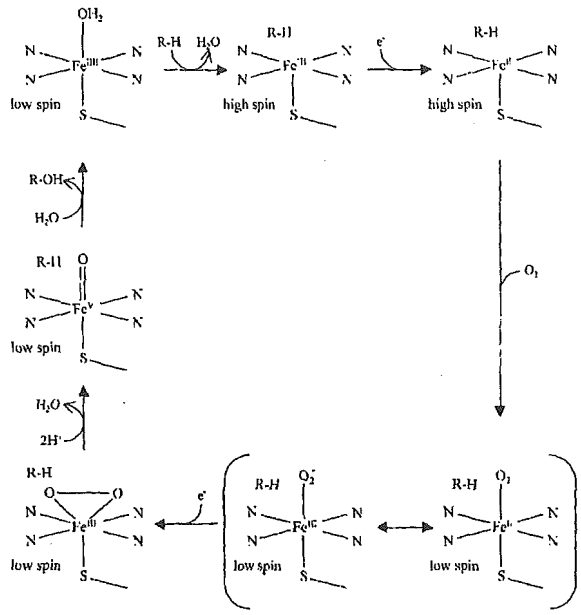

Figure 1. Catalytic cycle of P450s.

leads to an increase in the redox potential and, therefore, the enzyme can accept an electron from an electron-donor molecule such as NADPH or NADH. Fe(III) is thus reduced to Fe(II) and the catalytic reaction proceeds to the next step of the cycle. Substrate binding also generally causes a shift from a low- to a high-spin state. In P450cam from *Pseudomonas putida*, which metabolizes camphor, the redox potential increases from −300 mV to −173 mV on substrate binding.[10]

As previously mentioned, because high-spin five-coordinated Fe(III) is closely related to substrate binding, computational evaluation of this state is important in studies of the drugs and toxic agents that are docked into P450 enzymes. Recently, several iron–porphyrin complex models of P450s have been built using quantum chemistry methods. Complex models with six-coordinated iron,[11–13] and models with substrates or inhibitors, such as alkane, alkene, and nitric oxide,[14–18] have been examined using various computational methods, including Hartree–Fock calculations[19] and density functional theories.[13–18,20] However, there have been few studies on iron–porphyrin models with high-spin state five-ligated Fe(III).[19,20] Furthermore, there has been no systematic study of these five-coordinated Fe(III) iron–porphyrin models using different methods and basis sets.

To investigate the interaction between P450s and various small compounds in drug design trials, molecular mechanical (MM) calculations and classical molecular dynamics (CMD) simulations are generally suitable in terms of time and costs. Although simplified models are important for detailed investigations of the chemical properties of proteins, whole protein structures that are not simplified are indispensable in drug design investigations, such as docking studies on small molecules, virtual screening trials, and *de novo* design. Several quantum chemical methods and QM/MM methods for whole proteins have been developed,[21–23] but they are too computationally expensive to investigate large numbers of protein–ligand complexes, for example, in virtual screening. Therefore, MM and CMD calculations are the most suitable methods for drug design and development. Force field parameters are indispensable in MM and CMD methods, and parameters for molecules other than amino acids, such as heme, are often unavailable. Although sets of force field parameters for the heme moiety are available (http://pharmacy.man.ac.uk/amber/),[24] they are intended for calculations of hemoglobin, myoglobin, and cytochrome *c*, and are therefore not suitable for P450s. These parameters can be used for porphyrin rings, but parameters relating to axial ligands of the iron atom (that is, CYS) have not yet been determined. Furthermore, parameters only exist for heme with a six-ligated iron atom and those for heme with a five-coordinated iron atom, which plays an important role in the catalytic cycle of P450s, remain to be calculated. In addition to force field parameters, atomic charges are generally required for MM and CMD, and the electronic states need to be investigated in order to calculate these values.

Quantum chemical calculations with simplified models are generally used to determine parameters and atomic charges for MM and CMD. The results of quantum chemical calculations on iron–porphyrin simplified models can be used in MM and CMD calculations on whole P450s. In this way, it is possible to predict substrate binding modes and complete virtual screening trials for drug candidates. High-spin state five-ligated Fe(III), which is related to substrate binding, plays a significant role in these calculations.

In this study, models with five-coordinated Fe(III) are built for P450s and their accuracies are evaluated using geometry optimizations via various quantum chemical methods. Furthermore, we investigate which methods are most suitable for use with these models. The parameters and atomic charges that are indispensable in MM and MD calculations for P450s are also obtained.

Methods

The iron–porphyrin models used in this study are illustrated in Figure 2. Model 1 is a detailed model of a P450 enzyme, which includes the protoporphyrin IX with Fe(III) axially ligated through the sulfur atom of CYS. An acetyl group (ACE) and a methylamino group (NME) are bound to the amino (N)- and carboxy (C)-terminuses of CYS, respectively. Model 2 is more simplified and includes the porphyrin with Fe(III) axially ligated to the sulfur of a methylthio group. There are 95 and 42 atoms in models 1 and 2, respectively.

For each model, geometry optimizations were carried out using the following quantum chemical methods: semiempirical unrestricted Austin Model 1 (AM1); *ab initio* unrestricted Hartree–Fock (UHF) molecular orbital methods; and unrestricted hybrid density functional theory (DFT) combining five functionals—Hartree–Fock, Slater, and Becke exchange, and Vosko–Wilk–Nusair and Lee–Yang–Parr correlation terms (*UB3LYP*). 3-21G*, 4-31G*, 6-31G*, and Tatewaki–Huzinaga's MIDI[25] with Hay's diffuse d[26] basis sets were adopted. A different basis set was used for the iron atom in some of the calculations. Table 1 shows the